J. Fluid Mech. (2025), *vol.* 1015, A39, doi:10.1017/jfm.2025.10314

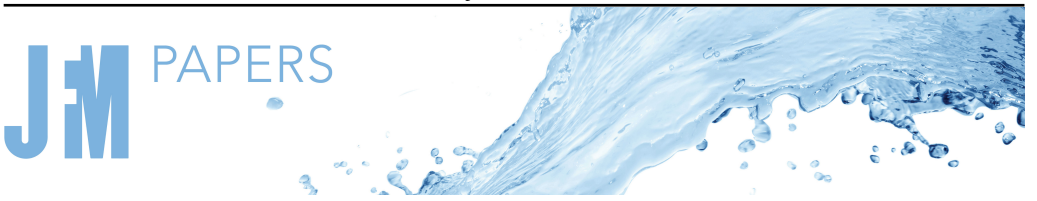

Wake merging and turbulence transition downstream of side-by-side porous discs

Fanny Olivia Johannessen Berstad[1], **R. Jason Hearst**[1] and **Ingrid Neunaber**[1,2]

[1]Department of Energy & Process Engineering, Norwegian University of Science & Technology, NO-7491 Trondheim, Norway

[2]FLOW Turbulence Lab, Department of Engineering Mechanics, KTH Royal Institute of Technology, SE-100 44 Stockholm, Sweden

Corresponding author: R. Jason Hearst, jason.hearst@ntnu.no

(Received 18 October 2024; revised 23 May 2025; accepted 26 May 2025)

The wake merging of two side-by-side porous discs with varying disc spacing is investigated experimentally in a wind tunnel. Two disc designs used in the literature are employed: a non-uniform disc and a mesh disc. Hot-wire anemometry is utilised to acquire two spanwise profiles at 8 and 30 disc diameters downstream and along the centreline between the dual-disc configuration up to 40 diameters downstream. The spanwise Castaing parameter profiles confirm the appearance of rings of internal intermittency at the outermost parts of the wakes. These rings are the first feature to interact between the discs. After this point, the turbulence develops to a state whereby an inertial range is observable in the spectra. Farther downstream, the internal intermittency shows the classical features of homogeneous, isotropic turbulence. These events are repeatable and occur in the same order for both types of porous discs. This robustness allows us to develop a general map of the merging of the two wakes.

Key words: wakes, intermittency

1. Introduction

The interaction of wakes has been studied in various contexts within fluid mechanics, *inter alia* interacting von Kármán vortex streets downstream of a pair of cylinders, wakes from different bluff bodies or tidal and wind turbine wakes.

To study such wake interactions, wind tunnel experiments are an important tool as specific wake features of different wake-generating objects can be scrutinised, e.g.

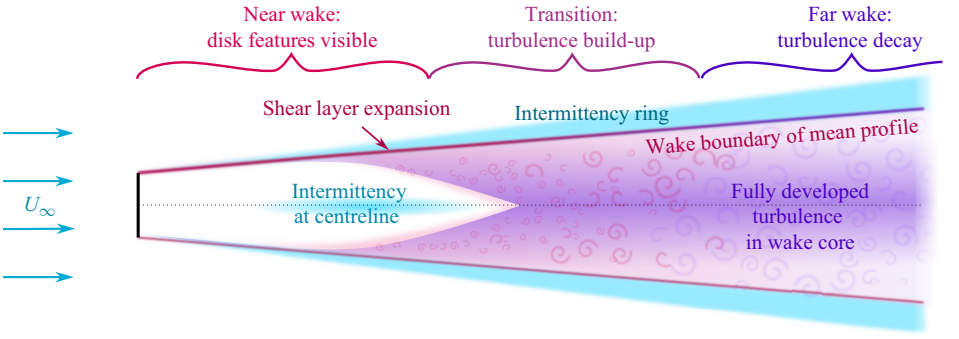

Figure 1. Schematic of the mean wake features evolving downstream of an axisymmetric (porous) object exposed to uniform inflow with a velocity of U_∞.

Strykowski & Sreenivasan (1990), Brown & Roshko (2012), Zhou & Mahbub Alam (2016), Li *et al.* (2020), Gambuzza & Ganapathisubramani (2023), Biswas & Buxton (2024), Cicolin *et al.* (2024) and Messmer, Hölling & Peinke (2024). Using the example of wind energy, the importance of wake effects becomes particularly clear as a wind turbine operating in the wake of an upstream turbine both produces less power and experiences higher fatigue loads (Thomsen & Sørensen 1999; Barthelmie & Jensen 2010).

Recently, wake-generating objects such as porous discs (PDs) or fractal discs have received attention both from the turbulence perspective, e.g. Obligado, Dairay & Vassilicos (2016), Vinnes *et al.* (2023), Bourhis & Buxton (2024) and Steiros *et al.* (2025), and in the context of wind energy, where PDs are used as simplified turbine models for wake studies, e.g. España *et al.* (2011, 2012), Aubrun *et al.* (2013), Theunissen, Allen & Housley (2015), Camp & Cal (2016), Bossuyt, Meneveau & Meyers (2018), Helvig *et al.* (2021), Neunaber *et al.* (2021) and Vinnes *et al.* (2022*a*). As Helvig *et al.* (2021) and later Kurelek, Piqué & Hultmark (2023) concluded, the design of the PD itself will have an effect on the wake and not all PD designs mimic the wake features of a wind turbine wake with the same fidelity. It is also worth noting that an axisymmetric porous body is a generalisation of a wake-generating object and hence the fluid mechanics they illuminate has consequences for a variety of geometries, e.g. wind turbines, trees, buildings, offshore underwater structures.

Flow close to the wake-generating object, such as a PD, exhibits features that depend on the object but these individual features diminish farther downstream. The general turbulence evolution in a wake can be classified by different stages, as illustrated in figure 1, which is a composite from classical texts, e.g. Tennekes & Lumley (1972) and Pope (2000), as well as contemporary research, e.g. Schottler *et al.* (2018), Neunaber *et al.* (2020, 2021), Vinnes *et al.* (2023), Bourhis & Buxton (2024), Cicolin *et al.* (2024), and Steiros *et al.* (2025). The addition of moderate turbulence levels (approximately 12 % or less) to the inflow does accelerate the wake evolution, but the typical stages of the wake development do not change (e.g. Wu & Porté-Agel 2012; Neunaber 2019; Neunaber *et al.* 2020, 2021; Vinnes *et al.* 2023; Bourhis & Buxton 2024). An important distinction here is the vortex shedding of PDs with non-uniform blockage in turbulent inflow with turbulence intensities above 5 %, where Bourhis & Buxton (2024) show that the vortex shedding diminishes; however, for the qualitative description here, this is secondary. In the near wake, the individual axisymmetric (porous) object features are visible and the shear layers between the faster ambient flow and the slower wake have yet to meet. The spanwise velocity deficit profile is pronounced and not yet Gaussian, and the spanwise turbulence intensity profile has two peaks marking the shear layers. The shear layers expand, and when

they meet, turbulence builds up and finally decays in the far wake, where the spanwise mean velocity profile has a Gaussian shape. A sufficiently developed turbulent flow has certain characteristics. One such characteristic is the appearance of a $k^{-5/3}$ region in the energy spectrum's inertial range, where k is the wavenumber. In principle, this region comes into existence once the turbulence has had time to shed its dependence of the initial conditions and has reached a 'universal' state (Frisch 1995). In the far wake, this state is reached and the fully developed turbulence shows classical decay, e.g. Neunaber *et al.* (2020, 2021). Another turbulence feature identified in both wind turbine wakes and PD wakes is the internal intermittency of the flow. The definition of internal intermittency employed herein refers to the probability of sudden and large changes of velocity in the flow, which can be described as the extreme events in a probability density function (PDF) of the velocity increments. Schottler *et al.* (2018) and Neunaber *et al.* (2020) identified a ring of intermittency at the edge of the wake of a wind turbine for cases with both near-laminar and turbulent inflow conditions. This was later verified for the same PDs used in the present investigation by Vinnes *et al.* (2023) both in near-laminar and turbulent flow. These three sets of authors discerned the ring of intermittency with the Castaing parameter, a quantification of the internal intermittency, and as is stated in these works, the ring lies outside the momentum-defined wake. In other words, this ring of intermittency is the outermost part of a PD wake, and cannot be identified using one-point statistics.

While many studies have been carried out to characterise the features of single wakes, comparatively few have been focussed on the interaction of axisymmetric wakes of side-by-side wake-generating objects and the emergent turbulence features. Several experiments have been done on wind turbine wake interaction with wind turbines in a tandem configuration, e.g. Schümann *et al.* (2013), Jackson & Amano (2017), Garcia *et al.* (2019) and Vad, Tamaro & Bottasso (2023), or small park arrangements (Camp & Cal 2016; Scott *et al.* 2020), but there is little research done on wake interaction between wind turbines or PDs that are side by side. An exception is Maus, Peinke & Hölling (2022), who experimentally investigated how lateral spacing and the rotational direction of two model wind turbines affect the wakes and their interaction at diameter-based Reynolds numbers ranging from 160 000 to 280 000. They used small lateral spacings, which are interesting for multi-rotor settings (e.g. Bastankhah & Abkar 2019). Interestingly, they found that, for lateral spacings in the range $1.07D$ to $2.00D$ centre to centre, D being the rotor's diameter, a decrease in lateral spacing caused an increase in generated power. They argue that the increased power generation is caused by flow acceleration through the middle of the dual-rotor set-up. Maus *et al.* (2022) also briefly discuss the use of the Castaing parameter to investigate the wake-interaction length for the two model wind turbines. By using 21 single-wire hot-wires in a laterally spaced array and measuring downstream, they collected data on the flow characteristics from $1D$ downstream up to $8D$ downstream, and argued that the wakes met where the two intermittency rings, i.e. the outermost parts of the wakes, met along the centreline. For their $1.5D$ turbine spacing case, the wakes met between $3.5D$ and $5D$, depending on the rotational direction of the turbines.

Recently, Obligado, Klein & Vassilicos (2022) looked into the wake merging of two plates in a wind tunnel. They used a set of square plates and a set of fractal plates, i.e. square plates where the periphery follows a fractal design. The Reynolds number based on the inflow velocity and the square root of the disc's frontal area was 43 000. Single-wire hot-wire anemometry measurements were obtained and analysed with the goal of calculating the wake-interaction length and relating their findings to existing scaling laws for equilibrium and non-equilibrium turbulence predictions. In their study, they define the wake-interaction length, x_{12}, from the streamwise distribution of the velocity fluctuations. Before the wakes meet, the streamwise distribution of the velocity fluctuations shows a

monotonic increase in the velocity fluctuations, and the distribution deviates from this linearity once the wakes meet. Through linear regression in the first region, they find x_{12} by defining it as the downstream position where the distribution starts to deviate from this monotonic increase. Obligado *et al.* (2022) further argue that the appearance of a region with $k^{-5/3}$-decay in the spectra of the velocities in the spatial region between two wake-generating objects would imply that the turbulence therein has reached a certain level of maturity. Since this turbulence is generated from these blocking objects themselves, this implies that their wakes have met.

Although the interaction of two axisymmetric wakes is sparse in the literature, investigations of the interaction of two, or more, planar wakes generated by cylinders has received a lot of attention over the past decades (see e.g. reviews by Zdravkovich 1977; Sumner 2010; Zhou & Mahbub Alam 2016). While there are also many studies on the interaction of a cylinder wake with the wake of a much smaller control rod, e.g. Strykowski & Sreenivasan (1990) and Cicolin *et al.* (2021), we will focus on studies with identical objects here. In particular, studies investigating the interaction of wakes of side-by-side cylinders classify three regimes that depend on spacing and Reynolds number. For spacings smaller than $1.2D$ centre to centre, a single wake emerges. For spacings between $1.2D$ and, depending on the Reynolds number, approximately $2.0D$ and $2.2D$, a large and a small vortex street are observed, and finally, for spacings between approximately $2.0D$ and $2.2D$ and $4.0D$ and $5.0D$, two coupled vortex streets evolve. For larger spacings, the wakes do not significantly interact. For the interaction of the wakes of two flat plates, a similar classification can be made, albeit with variations in the spacing where the three regimes are found, e.g. Dadmarzi *et al.* (2018). It should be emphasised that, while some conclusions can be transferred to the interaction of axisymmetric wakes, the flow features, and thus their interactions, are quite different.

The wake merging and transition to turbulence between two axisymmetric side-by-side wakes, such as those generated by PDs, is a topic that has not been extensively explored, and there is therefore no definite way in which the wake interaction is defined and it cannot be predicted *a priori*. For the wake merging works for side-by-side wind turbines or PDs that can be found in the literature, there is a discrepancy in what they define as wake interaction, which implies that there are many physical mechanisms at play during wake merging. For example, Obligado *et al.* (2022) determined wake interaction by means of the streamwise velocity fluctuations and the existence of an inertial range in the spectra, and Maus *et al.* (2022) suggest the assessment of intermittency via the Castaing parameter. In contrast to these turbulence-based definitions, wake superposition models define the merging based on modelling the mean velocity in the regions where the modelled mean velocity profiles interact (e.g. Lissaman 1979; Katic, Højstrup & Jensen 1987; Voutsinas, Rados & Zervos 1990; Niayifar & Porté-Agel 2016; Zong & Porté-Agel 2020; Bastankhah *et al.* 2021). The present study experimentally investigates the wake merging development of turbulence between two types of side-by-side PDs with similar drag and blockage but different wakes (Vinnes *et al.* 2022*a*, 2023) by means of different turbulence parameters to elucidate common features targeting three research questions:

(i) What is the influence of the disc spacing on the wake merging process?
(ii) What is a suitable measure to characterise the merging of wakes and development of turbulence?
(iii) Are the merging stages independent of the disc geometry?

Based on the schematic of the wake of a single axisymmetric wake-generating object, we hypothesise that:

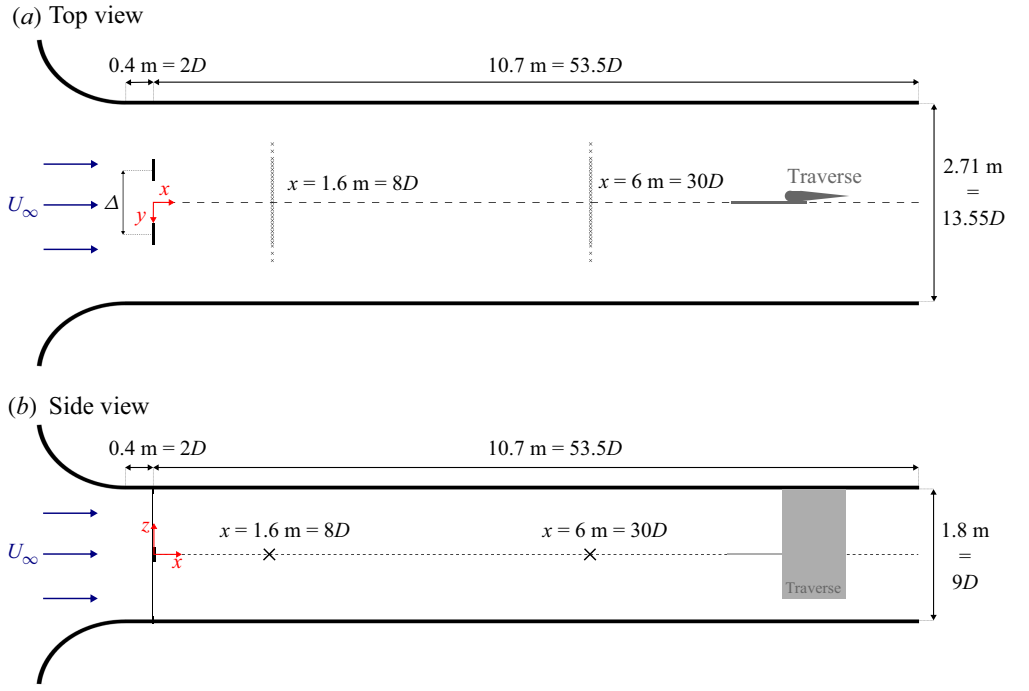

Figure 2. Wind tunnel schematics. (*a*) The wind tunnel seen from above. The spanwise measurement locations are marked with × in the y-direction. The disc spacing Δ is measured centre to centre. (*b*) The wind tunnel seen from the side. The spanwise measurements are marked by ×. The schematics are to scale except the discs, and the automated traverse is represented as the dark grey figures farthest downstream. The sloping roof is not explicitly shown.

(i) the disc spacing will influence the turbulence interaction as it influences where in their individual evolution process the two wakes will meet;
(ii) the intermittency ring will give a clear indication of first wake interaction;
(iii) the disc geometry will not change the fundamental evolution mechanisms but have an impact on the downstream position where the wakes meet.

The conclusions from these experiments will advance the understanding of turbulence interaction in wakes and how turbulence develops in this situation, which is relevant for, *inter alia*, wind farms, farms of tidal turbines, forest canopies, urban settings as well as fundamental understanding of the underlying turbulent processes.

2. Experimental methodology

The experiments took place in the large closed-loop wind tunnel at the Norwegian University of Science and Technology, which has a test section with dimensions 11.1 m × 2.71 m × 1.8 m. The height of the roof is gradually adjusted to 1.91 m in order to compensate for boundary layer growth and to keep the pressure gradient in the streamwise direction approximately zero. All experiments were conducted at an inflow velocity $U_\infty \simeq 10\ \mathrm{m\,s^{-1}}$ and a background turbulence intensity $< 0.3\ \%$. Figure 2 displays schematics of the wind tunnel set-up. These schematics are to scale, however, the roof height adjustment has been neglected for simplicity.

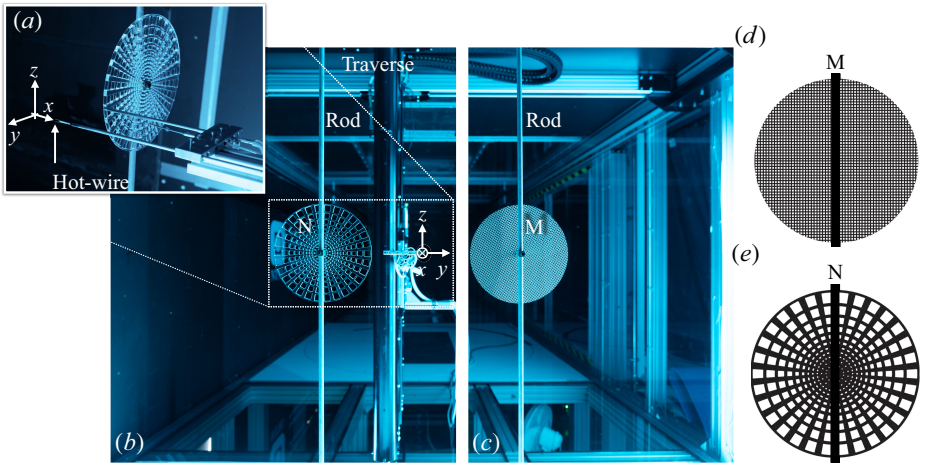

Figure 3. (*a*) Photograph of the hot-wire; (*b*) photograph of the non-uniform disc (N) in the wind tunnel with the traverse; (*c*) photograph of the mesh disc (M); (*d*) schematic of the M disc; (*e*) schematic of the N disc. The black rod through the discs represents the mounting rod. Note that a combined study, such as suggested by (*b*) and (*c*), is not part of this investigation, the discs are always of the same type.

The two PDs used in this study both have a diameter $D = 200$ mm, resulting in a Reynolds number of $Re = U_\infty D/\nu \approx 1.25 \times 10^5$, where ν is the kinematic viscosity. For comparison, the experiments of Obligado *et al.* (2022) were performed at $Re \approx 0.43 \times 10^5$. The discs are the same as those used in Vinnes *et al.* (2022*a*, 2023), where their individual wakes are documented (see also figures 4(*e*) and 4(*f*), figures 6(*e*) and 6(*f*), and schematics and a photograph of the set-up can be seen in figure 3. Both discs have a solidity of 57 % and a drag coefficient of $C_D \approx 0.8$ (Vinnes *et al.* 2022*a*). The non-uniform disc (N) has been cut from a 5 mm acrylic sheet, and has decreasing blockage with increasing distance from the centre; the technical drawing can be found in Vinnes *et al.* (2022*b*). The mesh disc (M) was made out of wire mesh with a thickness of 0.8 mm and a mesh size of 2.3 mm, and it has uniform blockage. A significant phenomenological difference in the wakes of the two PDs is that the N-type disc exhibits vortex shedding, while the M-type disc does not. The lack of vortex shedding has been reported for porous plates with uniform blockage below 0.72, cf. Castro (1971) and Cicolin *et al.* (2024). Recently, the vortex shedding of non-uniform discs with similar design has been investigated by Bourhis & Buxton (2024). Despite a similar solidity and drag coefficient, the wake of the M-type disc recovers significantly more slowly than that of the N-type disc (Vinnes *et al.* 2022*a*, 2023), both due to the small openings that do not shed energetic structures, yielding smaller integral length scales and less turbulent kinetic energy which hinders the recovery process (Kurelek *et al.* 2023), and because the lack of vortex shedding causes less mixing and a very late onset of self-similarity (Steiros *et al.* 2025).

In the present study, the PDs were mounted on rods spanning the entire height of the wind tunnel, unlike the studies of Vinnes *et al.* (2022*a*, 2023), where the discs were mounted on top of masts to mimic actuator disks or wind turbines. The present configuration prevents the wake of the discs from drifting down into the wake of the mast (Pierella & Sætran 2017). We expect the impact of the mounting rod on the measurements to be negligible for studying wake merging, as both discs act like flow homogenisers, as they are mounted downstream of the rods. Therefore, there are no large structures from the rod, and the turbulence generated by the discs diminishes the impact of the velocity deficit from the rod's wake rapidly downstream. In addition, for the N disc,

at the vertical centreplane, the disc has a 100 % blockage core and the disc was oriented in a way such that bars are aligned with the mounting rod to minimise additional blockage through the mounting. Therefore, we expect the effect of the mounting rods to be secondary, particularly for the focus on wake merging.

The discs were aligned with respect to the wind tunnel and each other by utilising an alignment laser with a wide opening angle positioned upstream by the mounting of the PDs and two reference points farther downstream. The model solid blockage of two discs in the wind tunnel is 1.3 %, and the blockage of the whole set-up, including the discs, rods and support structures is 6 %.

Hot-wire anemometry was used for all velocity measurements. A Dantec Dynamics 55P01 single-wire probe was used, with a sensing element of 1.25 mm. A Dantec Dynamics StreamLine Pro constant temperature anemometer operated the hot-wire. An automated traverse was employed for moving the hot-wire to different measurement positions. The accuracy of the traversing system is approximately ± 0.5 mm in both the x- and y-directions. The sampling time at each measurement point was $t_s = 180$ s, which corresponds to 9000 flow turnovers based on the mean velocity and disc size. A sampling frequency of $f_s = 75\,047$ Hz was used with a hardware low-pass filter of 30 000 Hz. In order to reduce the remaining high-frequency noise, an iterative digital low-pass filtering method (Mi *et al.* 2005, 2011) was used with a digital filtering frequency of $f_c = 1.1\, f_k$, where f_k is the Kolmogorov frequency. The Kolmogorov frequency was estimated by a fifth-order differential scheme in the same iterative process (Hearst *et al.* 2012). The hot-wire measurements were temperature corrected as per Hultmark & Smits (2010). The hot-wire was calibrated approximately every 4–5 hours, and a weighted average of the calibrations was used for the measurements taken in between the calibrations. In order to reduce temperature drift during measurements, the wind tunnel was run at high velocity for approximately an hour before conducting experiments. The presented measurement procedure results in a maximum random error, calculated by the method of Benedict & Gould (1996), of the mean velocity of 2.5 % or less, depending on the turbulence intensity, but can increase to around 4.6 % for single cases with very high turbulence intensities ($u'/U > 0.25$), e.g. for the N1.5 case at the centreline; the maximum random error of the turbulence intensity is 1 % or less. Mean velocities are converged within ± 0.5 % after 45 s; standard deviations are converged within ± 1.0 % after 120 s or earlier if the turbulence is developed at the respective position, if not (e.g. at the wake borders or close to the discs where the standard deviations are also very low), the convergence is within ± 2.0 %. Note that in general convergence and uncertainty are better in regions that are not subject to high intensity intermittent flow, i.e. the shear layers are more difficult to capture than the wake cores.

The wakes of two side-by-side M-type discs and two side-by-side N-type discs were investigated for three different spacings $\Delta = 1.5D$, $2.0D$ and $3.0D$ from centre to centre. These spacings allow us to investigate the merging of the wakes in different stages of their individual evolution, while also minimising interactions with the wind tunnel walls. The naming convention for the remainder of this work will refer to the disc configuration and the lateral spacing between the two discs. For example, M1.5 refers to the case with two M discs with a $1.5D$ spacing, and N3.0 refers to the case with two N discs with a $3.0D$ spacing. In addition, the wakes of both individual discs were measured in order to compare this with the dual-disc wakes. The wakes behind the PDs were measured at $8D$ and $30D$ downstream in the spanwise direction, as well as along the centreline in the streamwise direction from $0.5D$ to $40D$. In other words, a total of 24 measurement series were conducted for this study. For the streamwise scans, the hot-wire was positioned so that it coincided with the centre between the two discs. The spacings of the measurements were

Configuration	Discs	Δ/D	x_i/D	x_s/D	x_m/D
N	Single non-uniform	–	–	–	–
N1.5	Two non-uniform	1.5	1.8	2.0	3.2
N2.0	Two non-uniform	2.0	2.6	3.7	8.7
N3.0	Two non-uniform	3.0	5.2	8.3	–
M	Single mesh	–	–	–	–
M1.5	Two mesh	1.5	4.9	5.0	9.5
M2.0	Two mesh	2.0	11.0	12.7	31.5
M3.0	Two mesh	3.0	20.6	23.6	–

Table 1. Summary of test configurations. Here, x_i denotes the wake-interaction length determined by the shape parameter, i.e. where the wakes start interacting with each other, x_s denotes the downstream position where the centreline wavenumber spectrum reaches a near –5/3 slope in the inertial region, an indication that the wakes have merged, x_m denotes the downstream position where the wakes are merged with fully developed turbulence. A '–' indicates that the specific value was not obtained within the measurement domain. Specific definitions for x_i and x_m are provided in § 5, and for x_s in § 4.

adjusted for each case to capture relevant turbulence phenomena while simultaneously balancing the total acquisition time with the period over which the facility and calibration were thermally stable. Table 1 provides an overview of the test cases, as well as which discs were used with which disc spacing.

3. Wake characteristics

Before engaging in a detailed discussion of the wake merging process, we will first provide details on the first- and second-order statistics of the wake of the two-disc system to understand the context in which wake merging occurs. Note that, since a single-wire is used for the measurements, all presented quantities are based on the streamwise velocity. From these statistics, it is also possible to get an initial notion of where the wakes start to interact, i.e. 'feel' each other, and merge, characterised by turbulence that has reached a certain level of maturity.

3.1. *Mean velocity*

Figure 4 displays the normalised mean streamwise velocity measured across the spanwise direction at $8D$ and $30D$ downstream of the discs for all cases. If the normalised mean velocity at the centreline, $y/D = 0$, is lower than that of the free flow, $\bar{U}/U_\infty < 1$, this is a momentum-based indication that the wakes are interacting. Figures 4(a) and 4(c) show these profiles for the side-by-side N and M configurations, respectively, with different spacing between the discs, and figure 4(e) displays the mean velocity profiles for the single-disc cases for reference, all for $8D$. Figure 4(a) shows that the double wake of the N discs is wider than that of the M discs. Comparing the wakes in figures 4(a) and 4(c) with their respective single-disc counterparts in figure 4(e) shows that the wake merging will not only be influenced by the disc spacing, but it is also heavily influenced by the disc design as well, as the wake of the N disc is both wider and less pronounced than that of the M disc, which is in agreement with Vinnes *et al.* (2023). As mentioned above, this point is significant, as these two discs have the same drag coefficient, $C_D \approx 0.8$, but they still have different wakes and therefore wake merging. Using the drag coefficient as the only significant characteristic when replacing a wind turbine with a PD is therefore a limited approach, which was one of the main findings of Helvig *et al.* (2021) and later

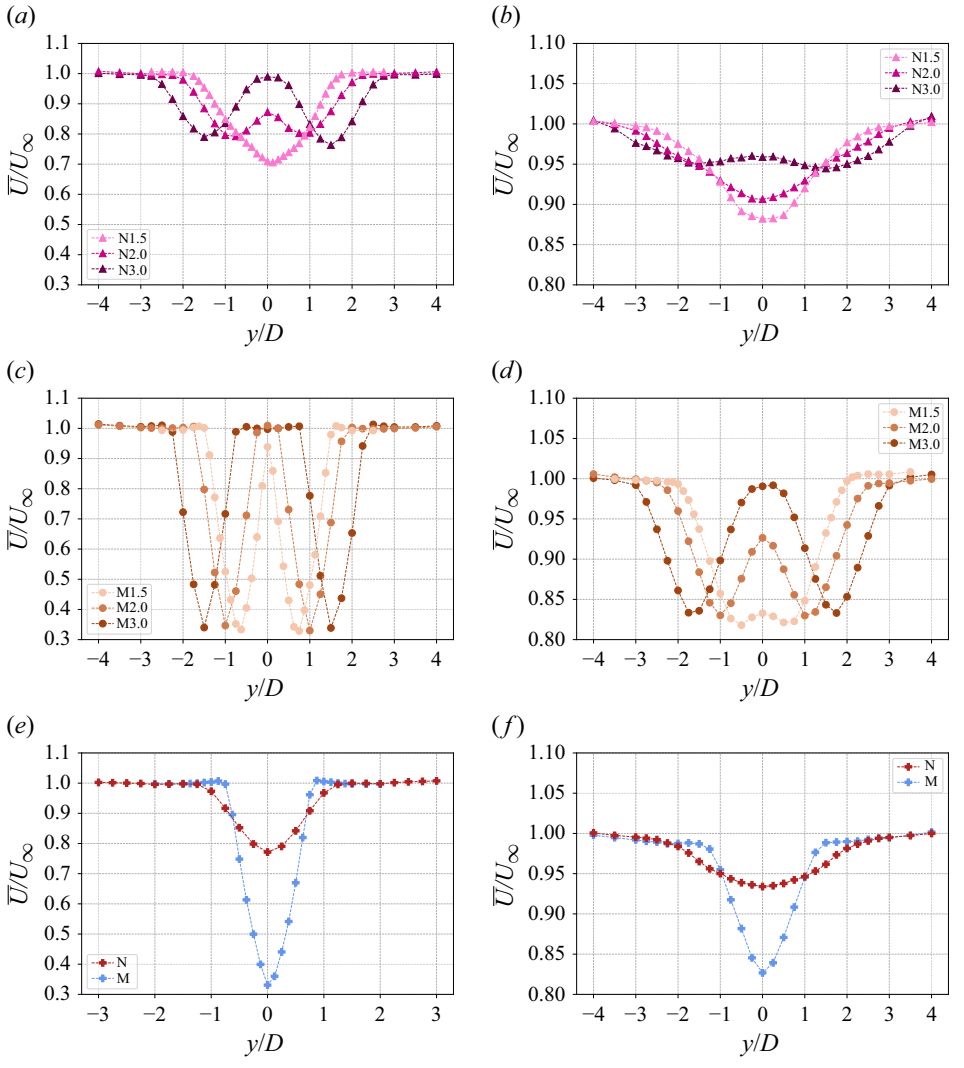

Figure 4. Evolution of the normalised mean streamwise velocity measured across the spanwise direction at $8D$ and $30D$ for all cases. The panels show the wakes of the N disc configurations at (*a*) $8D$ and (*b*) $30D$; the M disc configurations at (*c*) $8D$ and (*d*) $30D$; and the single-disc cases at (*e*) $8D$ and (*f*) $30D$. Note that the y-axes in the $8D$ and the $30D$ cases are scaled differently.

Kurelek *et al.* (2023). From the mean velocity profiles, we find that the side-by-side M disc profiles interact minimally at $8D$ and can be represented well by two single M disc wakes superimposed with different disc spacings; basic superposition of the wakes is illustrated in Appendix A. The same cannot be said for the N disc velocity profiles, where only the $3D$ disc spacing case, N3.0, appears as two single N disc wakes superimposed, cf. Appendix A. For the N2.0 case, it is still possible to discern two separate wakes, but the lower centre velocity suggests they have already started interacting. With N1.5, the two N disc wakes have already merged to a single velocity profile at $8D$ downstream with one distinct mean velocity minimum at $y/D = 0$. This combined velocity deficit is higher than the maximum velocity deficit of the single N disc. This demonstrates that the dual-disc configuration results in greater flow retardation than the single-disc case.

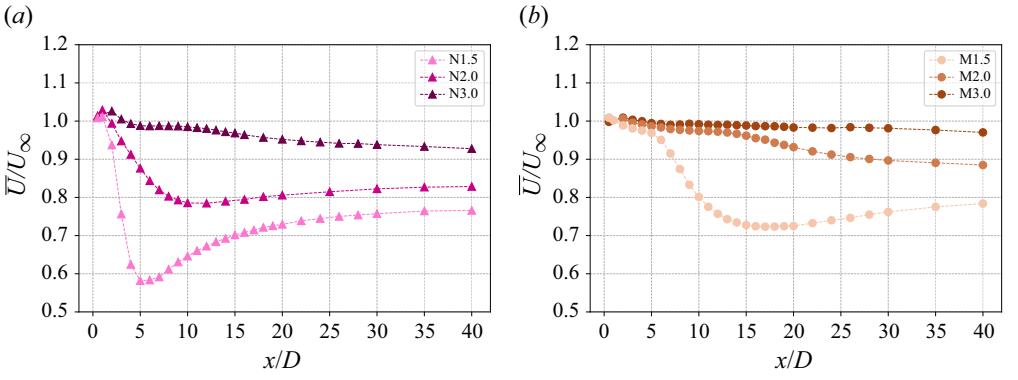

Figure 5. Evolution of the normalised mean streamwise velocity measured in the streamwise direction for all dual-disc cases. (*a*) The evolution for the N cases; (*b*) the evolution of the M cases.

Figures 4(*b*), 4(*d*) and 4(*f*) show the same velocity profiles as discussed above, but at $30D$ downstream from the discs. As expected, all wake velocity profiles are wider and have smaller gradients farther downstream due to entrainment. By comparing the single M disc wake in figure 4(*f*) with the M3.0 case in figure 4(*d*), we can conclude based on the mean velocity profiles that these wakes have yet to interact even at $30D$ since they are identical to the single-disc wake both in shape and velocity magnitude. The M1.5 and M2.0 cases in figure 4(*d*) both show that the wakes have started to interact and merge, since the mean velocity at $y/D = 0$ is decreasing. Using the same reasoning, the wakes in the N3.0 case in figure 4(*b*) interact but have yet to fully merge as well. As indicated, a simple possibility to find where turbulence interaction plays an important role in the merging process is to compare the superposition of the mean velocity profiles of the single discs with the measured profiles (see Appendix A). For the mean velocity profiles, superposition is a reasonable approximation at both $8D$ and $30D$ for cases where the wakes do not meet close to the PDs, i.e. with the exception of the N1.5 and N2.0 cases.

Figure 5 displays the mean velocity, normalised by the velocity at the first measurement position, along the centreline, with the N disc cases in figure 5(*a*) and the M disc cases in figure 5(*b*). The N1.5 case in figure 5(*a*) has a strong gradient just downstream of the discs, and the mean velocity slowly recovers, but even at $40D$ downstream, a pronounced velocity deficit remains. The N2.0 case has a weaker gradient than the N1.5 case, while the N3.0 case does not exhibit this behaviour but has a weak velocity decline downstream of the discs. As seen in figure 4, the N configurations have wide wakes, which means they will meet earlier in their spatial evolution. For the N1.5 case, the discs are placed close enough together that their individual wakes start interacting almost immediately downstream of the discs. At this point in the flow, there is a strong shear layer between the wake and the free stream, and the turbulence production within the individual wakes is still high. It is worth reiterating that each wake has a characteristic evolution on its own, including turbulence build-up and decay, cf. figure 1. Depending on the disc spacing, the two wakes will meet either in a region with high turbulence production, such as in the N1.5 case, as will be discussed in §§ 3.2, or in a region where the single wakes are already decaying. We see a strong gradient in figure 5 for the N1.5 case, since the wakes meet while the turbulence production is still high. This argument can be extended to the N2.0 case, although it has a weaker gradient than the N1.5 case, the individual disc wakes still meet early in their evolution where the wakes have not decayed significantly. For the N3.0 case, however, the disc spacing is large enough that, despite a wide wake width, the wakes meet sufficiently

far downstream such that the wakes have initiated their decay before they start interacting such that we observe a 'soft' merging, indicated by a gradually decreasing velocity. In figure 5(*b*), the M1.5 case shows a similar trend to the corresponding case in figure 5(*a*), only farther downstream and with a less steep gradient. The same can be said for the M2.0 case, but for the M3.0 case there are no significant changes in the magnitude of the mean velocity, further confirming that in this case the wakes of the two M discs have, for this parameter, not started to significantly interact within the measurement domain. In other words, the M configurations follow the same trend as the N configurations, but differ in that the M disc wakes meet farther downstream.

3.2. *Turbulence intensity*

The turbulence intensity was calculated by dividing the standard deviation of the streamwise velocity fluctuations, u', by the local mean streamwise velocity, U. Figure 6 shows the spanwise $u'/U(y)$ profiles for all cases at $8D$ and $30D$ downstream. If the turbulence intensity at the centreline exceeds the value of the background flow, $u'/U(y=0) > 0.3\,\%$, this is a turbulence-based indication that the wakes are interacting. The maximum magnitude of the spanwise $u'/U(y)$ profiles coincides with where the largest velocity deficit is for the fully merged wake profiles in the N1.5 case at $8D$, and the N1.5 and N2.0 cases at $30D$. For the other cases, the identities of the single wakes are still recognisable to varying degrees so that the maximum magnitude of the spanwise $u'/U(y)$ profiles is in the (inner) shear layer. The magnitude of the spanwise turbulence intensity profiles, $u'/U(y)$, decays in all cases between the $8D$ and $30D$ scans. Note that the y-axes of figure 6 for the cases at $8D$ and the cases at $30D$ are scaled differently. Comparing the dual-disc configurations with their single-disc counterparts, one can see that the magnitude of the spanwise $u'/U(y)$ profiles is roughly the same, regardless of disc spacing. The only exception is the N1.5 case, where the $u'/U(y)$-peak at $y/D=0$ is slightly larger than its maximum value for the single N disc at both $8D$ and $30D$ downstream. This is due to the wakes meeting relatively close to the discs in this case, where the turbulence production for the individual wakes is high as well. The degree to which simple superposition of the spanwise $u'/U(y)$ profiles of the single discs matches the measured side-by-side wakes is illustrated in Appendix A. For the spanwise $u'/U(y)$ profiles, simple superposition gives strong agreement in the case of little wake interaction (i.e. N2.0, N3.0, M1.5, M2.0, M3.0 at $8D$, and M3.0 at $30D$), but overestimates the magnitude in the centre of merged wakes (N1.5 at $8D$ and N1.5, N2.0, N3.0, M1.5 and M2.0 at $30D$).

Displayed in figure 7 is the evolution of the streamwise $u'/U(x)$ profiles for all dual-disc cases. Both configurations show higher values of the streamwise $u'/U(x)$ profiles for smaller disc spacings, but differ in magnitude. From $1.5D$ to $2D$ the peak magnitude of the streamwise $u'/U(x)$ profiles for both configurations is halved. Also, the maximum value of the streamwise $u'/U(x)$ profiles for the N1.5 case is almost thrice the maximum $u'/U(x)$ value for the M1.5 case.

Based on both the spanwise and centreline turbulence intensity profiles, it is possible to get a crude notion of how the wake merging occurs for the different dual-disc cases. The approach of Obligado *et al.* (2022) to quantifying the wake-interaction length through linear regression in the monotonically increasing region before the wakes merge requires a higher number of measurement points in this region than were acquired in the present study. Duplicating their approach was not an objective here, and other means of assessing wake interaction are considered in the subsequent sections. Nonetheless, the $u'/U(x)$ peaks in the centreline measurements can be considered a first indication of wake merging, as the start of the decay of the turbulence intensity indicates that the wakes have merged.

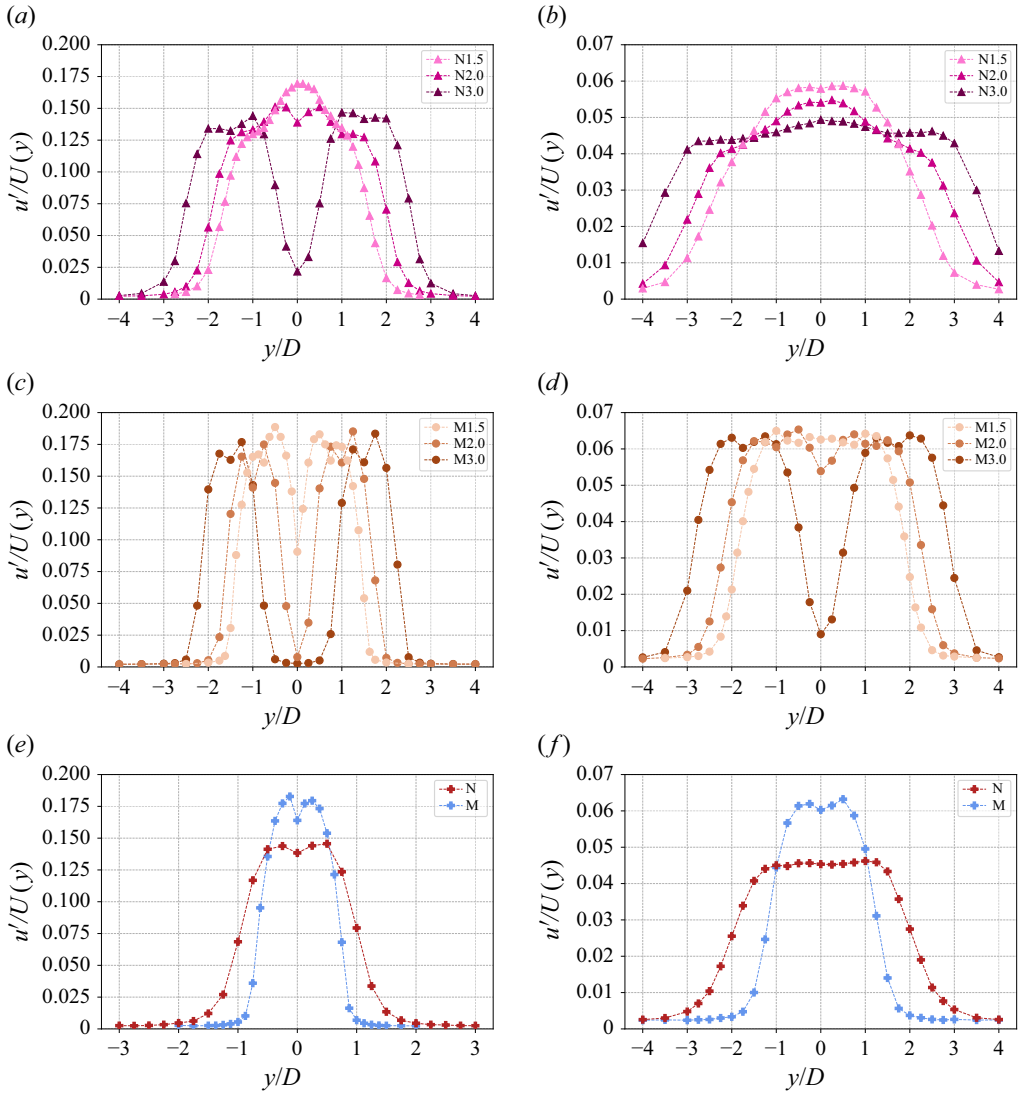

Figure 6. Evolution of $u'/U(y)$ profiles measured across the spanwise direction at $8D$ and $30D$ for all cases. The panels show the the spanwise $u'/U(y)$ profiles of the N disc configurations at (*a*) $8D$ and (*b*) $30D$; the M disc configurations at (*c*) $8D$ and (*d*) $30D$; and the single-disc cases at (*e*) $8D$ and (*f*) $30D$. Note that the y-axes in the $8D$ and the $30D$ cases are scaled differently.

For M2.0 and M3.0, the wakes start to interact and merge where the turbulence intensity of the single discs is already decaying since their wake width is smaller, which again leads to a smaller peak of the streamwise $u'/U(x)$ profiles along the centreline compared with their N disc counterparts.

4. Development of a spectral inertial range between the discs

A classical way to assess the development of a turbulent flow is to monitor the establishment of an inertial range in the spectrum. Close to the discs, the flow is near laminar at the centreline (cf. figure 7) and the spectra have low energy across all

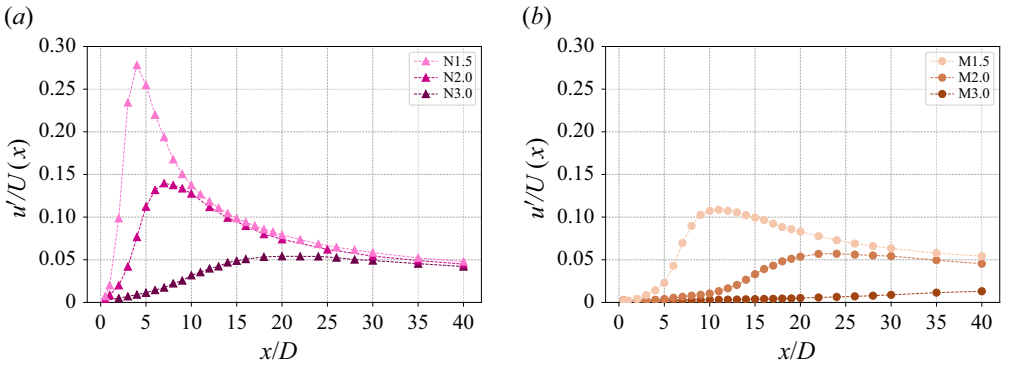

Figure 7. Evolution of the streamwise $u'/U(x)$ profiles at the centreline for all dual-disc cases. (*a*) The centreline profiles for the N disc cases; (*b*) the centreline profiles for the M disc cases.

frequencies and do not exhibit the classical shape of a turbulence spectrum with an established inertial range. When the wakes start to interact, the turbulence also starts to develop until it is mature and develops an inertial range with the classical $-5/3$ decay. Therefore, by identifying when an inertial range with $-5/3$ decay has been established, one can conclude that the wakes have merged sufficiently. Note that this method of identifying the interaction of wakes tracks the transition to turbulence from a non-turbulent state, and thus a similar approach would be more nuanced if the background flow was already turbulent, as one would seek a change in the turbulence structure rather than the development of turbulence. As will be detailed later in § 5, fully developed turbulence would also require the flow to exhibit internal intermittency only at small scales.

As can be seen in figure 7, initially, the inflow is near laminar at the centreline (background turbulence intensity of 0.3 %). Once turbulence is introduced along the centreline, it implies that the two wakes have started to interact. While turbulence along the centreline indicates the presence of wake interaction, it is not until the turbulence has had sufficient time to interact and mature (Obligado *et al.* 2022) that the inertial range of the turbulence spectrum exhibits the classical $-5/3$ power-law relation.

Figure 8 shows the flow development from near-laminar to interacting turbulent wakes to merged wakes with an established spectral inertial range with $-5/3$ decay in the two-disc configurations with $2D$ spacing. Figures 8(*a*) and 8(*c*) are velocity spectra in frequency space, whereas the figures 8(*b*) and 8(*d*) are compensated wavenumber velocity spectra. Plotting the wavenumber spectra in the compensated form is a way to emphasise the $k^{-5/3}$ power law which should appear as a plateau when such a range is achieved. Figure 8(*b*) shows compensated wavenumber spectra for N2.0, and figure 8(*d*) shows compensated wavenumber spectra for M2.0. At the first measurement point, $x/D = 0.5$, both configurations exhibit spectra of near-laminar flow that have low energies and lack the characteristic developed inertial range of turbulent flows. At $x/D = 2$ for the N2.0 case and $x/D = 8$ for the M2.0 case, the flows have gone from the near-laminar behaviour to starting to exhibit some properties of classic turbulent flow, as can be seen by increased energy and the start of the development of an inertial range. However, the gradients in the inertial range are still too steep. At the measurement point $x/D = 10$ for the N2.0 case and $x/D = 18$ for the M2.0 case, the flows have an established spectral inertial range that follows the $-5/3$ power law closely in the inertial range, since they are now approximately straight lines with zero slope in the compensated wavenumber spectra. It can also be noted that spectra after these downstream positions do not alter in shape, but either collapse with each other or exhibit turbulence decay through a shorter inertial range and a decrease

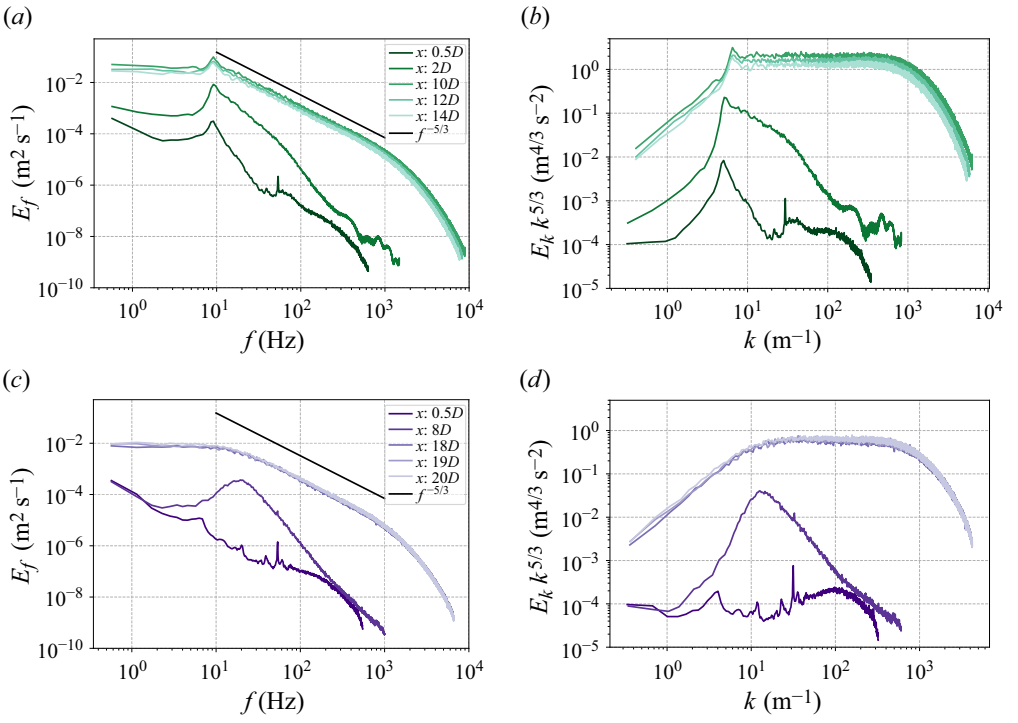

Figure 8. Spectra examples for different centreline measurements downstream of the discs. Spectra for N2.0 in (*a*) frequency space and (*b*) compensated wavenumber space. Spectra for M2.0 in (*c*) frequency space and (*d*) compensated wavenumber space. The axes are left dimensional to show the increase in the separation of scales and the magnitude of the kinetic energy dimensionally.

in energy. As can be seen in figures 8(*a*) and 8(*b*), the N discs exhibit vortex shedding as previously characterised by Vinnes *et al.* (2022*a*), as identified by the peak in the spectra at low frequencies.

In order to determine where the threshold between interacting wake turbulence and turbulence with an established spectral inertial range is, the evolution in the streamwise direction of the compensated wavenumber spectra is explored in more detail. First, for each case, spectra for all downstream centreline measurements were calculated and a moving average with equally spaced frequency interval in log space was applied (Fuchs *et al.* 2022). The approximate centre of the inertial range of a measurement was determined using the Taylor micro-scale, that was calculated by estimating the gradients using Taylor's hypothesis and a seventh-order centred-difference scheme as described by Hearst *et al.* (2012). From this point in the spectrum, starting with 5 points, linear regression is performed on $\log\left(E(k)\cdot k^{5/3}\right) = a + S\cdot\log k$. The fit range was extended in steps of 10 points towards higher wavenumbers as long as the fit error for the slope S decreases. Next, in a similar manner, the fit range was also extended to lower wavenumbers. Note that while a Taylor micro-scale can be calculated and a line can be fit to all spectra, including near-laminar cases, both only have a physical meaning in the case of turbulent flows. As is most clear in figure 8(*b*), the range of wavenumbers where the slope is close to zero within the inertial range depends on the downstream position. This is because the flow reaches a maximum turbulent kinetic energy value during mixing of the two individual wakes along the centreline, before the turbulent kinetic energy starts to decay downstream of the maximum point. The slope at each measurement position was then used as the parameter

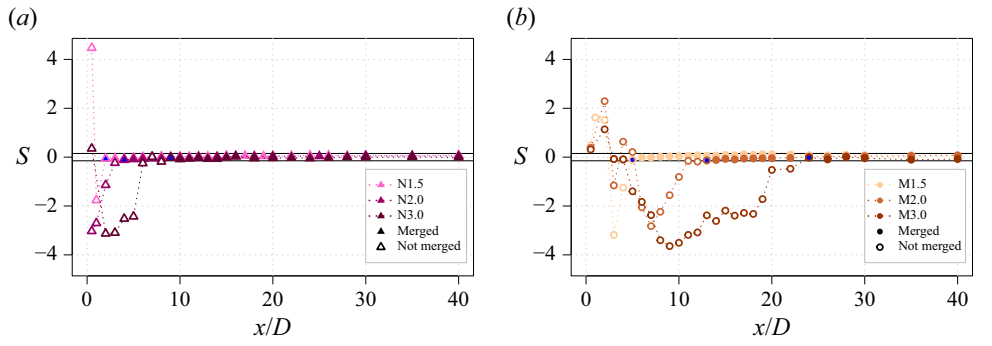

Figure 9. Slope within the inertial range of the compensated wavenumber spectra for (*a*) the N configurations and (*b*) the M configurations. Thresholds (± 0.15) are marked with black lines. Empty symbols are used to identify positions before wake merging, and filled symbols identify where the slope is within the threshold, i.e. where the wakes have merged. The first downstream position where the slope is within the threshold is marked with a blue filled symbol. The root mean square error at each measurement point is contained within the marker size.

for identifying if an inertial range was present. A threshold on the linear regression slope, S_{th}, was chosen for determining whether the turbulence at a measurement point fulfilled the $-5/3$ criterion in the inertial range or not. This threshold was used for all cases, and was chosen to be $S_{th} = \pm 0.15$ which is approximately 10 % of $-5/3$. The threshold was chosen to be small, while also inclusive of the final state of each case at the most downstream position.

The results of this endeavour can be seen in figure 9. The figure displays the slope within the inertial range as a function of downstream distance of the discs for both configurations and with the three different disc spacings. The first downstream measurement point where the slope threshold criterion is fulfilled is marked with a symbol with blue filling. Generally, the side-by-side N disc configurations reach an established spectral inertial range with an average extension of half a decade and with $-5/3 \pm 0.15$ decay for all disc spacings in a short distance downstream of the bodies, i.e. within $10D$ downstream. This is in stark contrast to the side-by-side M disc configurations, which require up to $24D$ downstream to achieve a mature state as determined by the appearance of an inertial range that also has an average extension of approximately half a decade. A summary of the identified locations is provided in table 1 as x_s. These values were found through linear interpolation between the first measurement point that fulfilled the slope criterion and the closest measurement point upstream of that. It should be noted that the slopes determined in the near field close to the discs should be interpreted with care as there is no clear inertial range, see also figure 8.

5. Wake merging as identified by internal intermittency

Another physical mechanism at play during wake merging is internal intermittency. As explained in the introduction, it has been shown that wakes, both in near-laminar and in turbulent inflow, are surrounded by a ring of high internal intermittency (cf. figure 1 and Schottler *et al.* 2018; Neunaber 2019; Vinnes *et al.* 2023), and we hypothesise that these rings are the first parts of the wake that will meet as they exist outside of typical wake width descriptions. The definition of internal intermittency employed herein refers to the probability of sudden and large changes of velocity in the flow, which can be described as the extreme events in a PDF of velocity increments. These sudden velocity

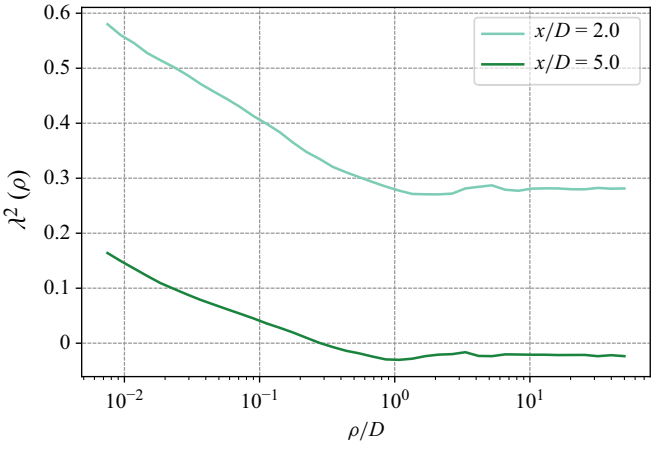

Figure 10. The Castaing parameter across multiple spatial scales ρ for N1.5 at two downstream positions. At $x/D = 2.0$, high values of intermittency can be observed across all scales, indicating the turbulence is still developing. At $x/D = 5.0$, there is some intermittency, but this is restricted to the smaller scales; this is typical of fully developed turbulence.

fluctuations would not be detected by use of only one-point statistics, therefore two-point statistics are necessary. For calculating the degree of internal intermittency in the flow, the central velocity increment is used. It is defined as $\delta u_\tau(t) = u(t - \tau/2) - u(t + \tau/2)$, and describes the velocity difference between two different points in time, their separation represented by a time scale τ. While the intermittency can be investigated through the moments of the central velocity increment (Toschi *et al.* 1999; Pope 2000), δu_τ^n, several investigations have estimated the internal intermittency from the Castaing parameter $\lambda^2(\tau)$, e.g. Peinke *et al.* (1993), Naert *et al.* (1994), Schottler *et al.* (2018), Neunaber *et al.* (2020), Maus *et al.* (2022) and Vinnes *et al.* (2023). The Castaing parameter is a quantification of the deviation of the PDF of the velocity increments, $p(\delta u_\tau(t))$, from a Gaussian probability distribution. If $\lambda^2 > 0$, then the flow has a higher probability of experiencing large changes in the velocity increments. It was introduced by Castaing, Gagne & Hopfinger (1990) as a shape parameter of the probability density distribution of the velocity increments, and Chilla, Peinke & Castaing (1996) showed that a simplified calculation is possible for fully developed turbulence

$$\lambda^2(\tau) = \frac{\ln(F(\delta u_\tau(t))/3)}{4}, \tag{5.1}$$

where $F(\delta u_\tau(t))$ is the flatness of the velocity increments. In this work, we will use the spatial equivalent of τ, ρ, by utilising Taylor's frozen flow hypothesis to convert the time scale to a spatial scale. The two line plots in figure 10 represent the Castaing parameter $\lambda^2(\rho)$ at two downstream positions along the centreline, $x/D = 2$ and $x/D = 5$, for the N1.5 configuration across multiple spatial scales ρ. Fully developed turbulent flows typically have both an established spectral inertial range with –5/3 decay and some internal intermittency for small scales ρ, here $\rho \lesssim D$, that decays according to a power law, and diminishes to zero for large scales, here $\rho \gtrsim D$. This is what we see at $x/D = 5$. For $x/D = 2$, however, we see large values of $\lambda^2(\rho)$ across all scales, indicating that at this downstream position the flow is not yet fully developed.

In terms of wake merging, detection of internal intermittency can be used for identifying the starting point for when the two wakes start interacting, x_i, and the end point where the turbulence in the centre of the two wakes is fully developed, x_m. Since the centreline

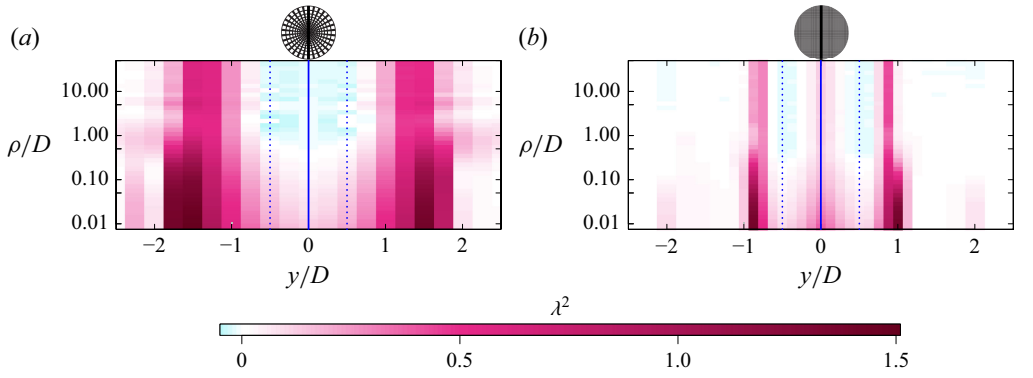

Figure 11. Contour plots of the Castaing parameter $\lambda^2(\rho)$ across spatial scales ρ in the spanwise direction at $8D$ downstream for the single-disc cases: (*a*) N, and (*b*) M. Increasing darkness indicates a higher $\lambda^2(\rho)$ value and thus a higher probability of extreme events. The blue solid lines indicate the centres of the discs while the blue dotted lines indicate the disc edges.

measurement is done exactly in the middle of the two discs, the evolution of the initial individual wakes should be symmetric, which is confirmed in § 3 for both the mean velocity and the turbulence intensity. As shown by Vinnes *et al.* (2023), both disc designs show a ring of intermittency outside the momentum-defined wake, and therefore observing the intermittency rings from the two discs meeting at the midpoint between them would be the first indication of any wake interaction. Figure 11 shows the Castaing parameter contour plots for the single-disc cases at $8D$ and their variation in the spanwise direction. Here, $\lambda^2(\rho)$ is the contour parameter, and increasing darkness indicates a higher probability of extreme events. The bands on the outer edges of the discs across all spatial scales indicate the presence of intermittency rings. Since Schottler *et al.* (2018) showed that there is a ring of intermittency, the spanwise profiles in figure 11 can be interpreted as a ring, although the measurement was done in one spatial dimension. For both single-disc cases, distinct bands can be observed, in agreement with the findings of Vinnes *et al.* (2023) of an intermittency ring on the outer edges of both discs' wakes.

Figure 12 displays Castaing parameter contour plots for all dual-disc cases at $8D$ downstream and their variation in the spanwise direction. For the M2.0 and M3.0 cases in figures 12(*d*) and 12(*f*), respectively, it is possible to discern clear and individual intermittency rings for both discs. For the M1.5 case in figure 12(*b*), however, the outer bands of both discs are visible, and a thin and weaker band is identifiable between the discs. This is due to the fact that wakes of the M discs have already started interacting. The side-by-side N configurations show a similar trend, but with overall higher $\lambda^2(\rho)$ across all spatial scales and over a larger spanwise length. For the N1.5 and the N2.0 cases in figures 12(*a*) and figure 12(*c*), respectively, no trace of the individual intermittency rings can be found, as the wakes in these configurations have already started to merge or, respectively, have already merged in the N1.5 case. With a disc spacing of $3D$ with the N discs, however, the lateral distance is large enough that at $8D$, a clear band is visible between the discs in figure 12(*e*).

To create a clear link between intermittency and wake merging, we chose to look closer into $\rho/D = 1$, i.e. a spatial scale of the same order of magnitude as the disc diameter D, at the centreline. We define the start of the wake interaction, x_i, when the Castaing parameter at this spatial scale exceeds $\lambda^2(\rho = D) > 0.2$. This value was chosen as the flow is clearly intermittent. Note that very large values of $\lambda^2(\rho) \gg 0.3$ should be interpreted with care as this is an indication of not fully developed turbulence (cf. Appendix A in Vinnes *et al.*

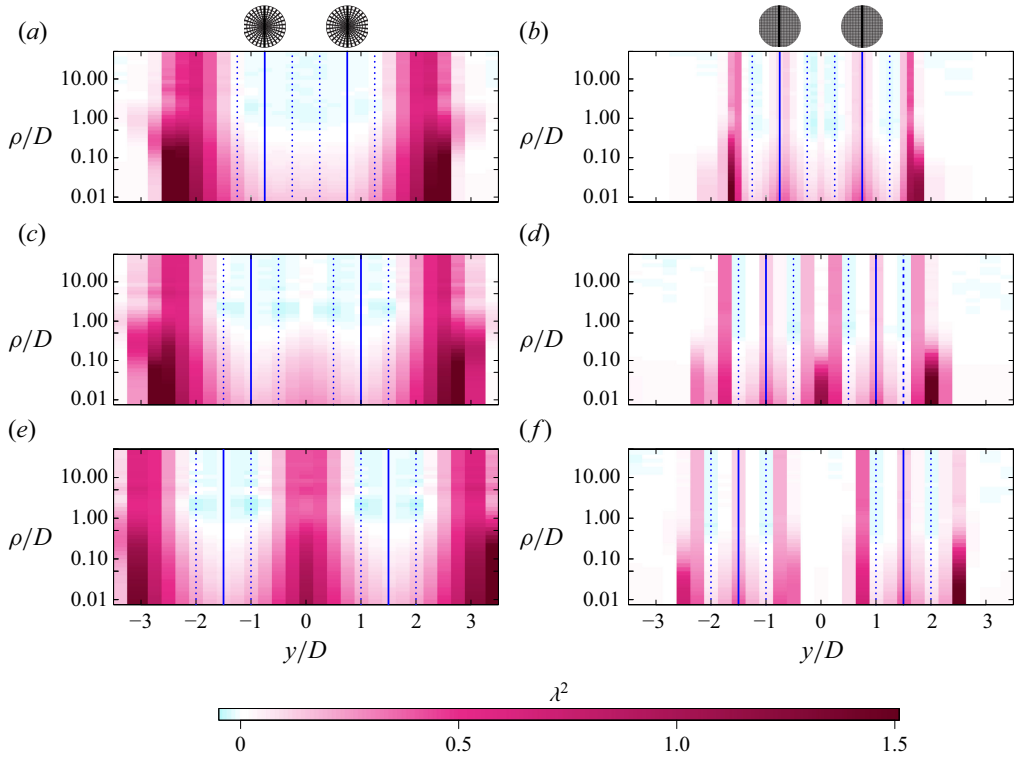

Figure 12. Contour plots of the Castaing parameter $\lambda^2(\rho)$ across spatial scales ρ at $8D$ downstream for the dual-disc cases: (*a*) N1.5, (*b*) M1.5, (*c*) N2.0, (*d*) M2.0, (*e*) N3.0 and (*f*) M3.0. Increasing darkness indicates a higher $\lambda^2(\rho)$ value and thus a higher probability of extreme events. The blue solid lines indicate the centres of the discs while the blue dotted lines indicate the disc edges.

2023). Extending this argument further, x_m is defined as when the Castaing parameter at the spatial scale $\rho/D = 1$ has decreased back to $\lambda^2(\rho = D) = 0$, where no internal intermittency is present at these scales. The results of this analysis can be seen in table 1. These values were found through linear interpolation between the measurement point that fulfilled the given internal intermittency criterion and the closest measurement point upstream. It should be noted that the sequence of wake merging events identified by the inertial range of the spectra and the Castaing parameter give consistent results for all cases, as can be seen in table 1. First, the intermittency rings interact, marked by x_i, then the spectra exhibit an inertial range, marked by x_s, and finally, the turbulence becomes fully developed, as indicated by x_m.

The downstream evolution of the Castaing parameter is plotted in dependence of ρ in figures 13 and 14. Figure 13 presents the Castaing parameter for the single discs, whereas figure 14 presents the Castaing parameter for the dual-disc configurations. Other spatial scales than $\rho/D = 1$ are included to emphasise the point made earlier about how high internal intermittency values across all scales is yet another indication that the flow is not fully developed. Figure 13 reveals that the disc design impacts the downstream position where the intermittency reaches its maximum, with the N disc design impacting the flow almost immediately downstream of itself, while the M disc design does not significantly influence the intermittency until approximately $7D$ downstream due to the narrow shear layers.

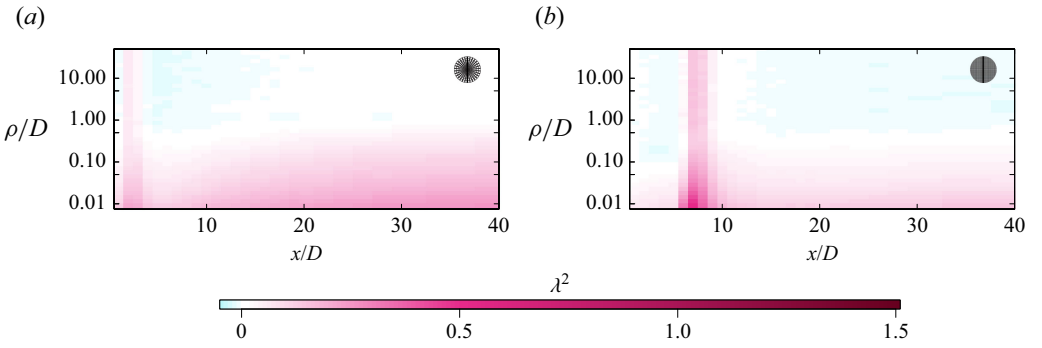

Figure 13. Castaing parameter contour plots for downstream positions along the centreline for the single-disc cases: (*a*) N, and (*b*) M. Increasing darkness indicates a higher $\lambda^2(\rho)$ value and thus a higher probability of extreme events.

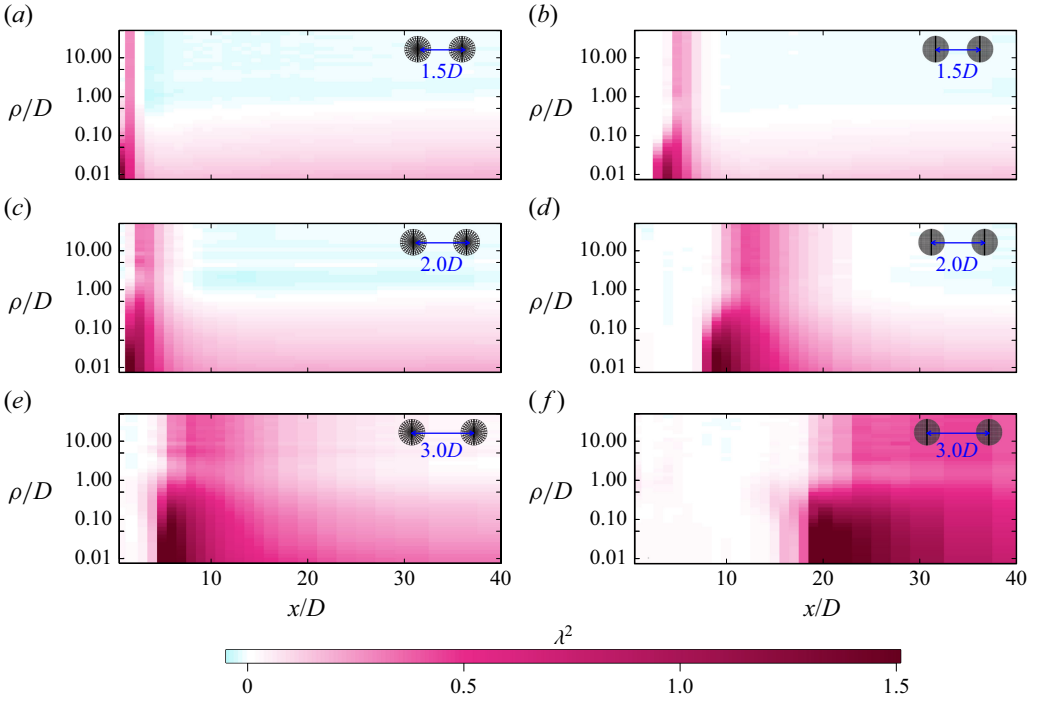

Figure 14. Castaing parameter contour plots for downstream positions along the centreline for the dual-disc cases: (*a*) N1.5, (*b*) M1.5, (*c*) N2.0, (*d*) M2.0, (*e*) N3.0 and (*f*) M3.0. Increasing darkness indicates a higher $\lambda^2(\rho)$ value and thus a higher probability of extreme events.

As can be seen in figures 14(*a*), 14(*c*) and 14(*e*), where the internal intermittency results for the dual-N cases are presented, the wakes start interacting almost immediately for the N1.5 case at $2D$ downstream, closely followed by the N2.0 case where the wakes start interacting at $3D$ downstream. After the wake interaction starts, the flow in these cases quickly converges downstream to fully developed turbulence with $\lambda^2(\rho > D) \approx 0$, while there is still intermittency present at the smallest spatial scales $\rho < D$. This does not happen for the N3.0 case, where the wakes start interacting at $4D$, and $\lambda^2(\rho) > 0$ for all spatial scales ρ downstream of $4D$. With the logic previously presented in this

section, the N3.0 case has therefore yet to become fully developed turbulence within the measurement domain. Figures 14(*b*), 14(*d*) and 14(*f*), show that the internal intermittency for the dual-M discs evolves differently. While the start of the wake interaction happens at a later downstream position compared with their N counterparts, the downstream lengths for when the Castaing parameter converges are also longer. In fact, for the M3.0 case, internal intermittency is still present within the measurement domain across all spatial scales, just like for the N3.0 case. The presence of intermittency at larger spatial scales $\rho > D$ indicates, as stated previously, that the turbulence has yet to reach its fully developed state. In other words, neither dual-disc wake with $3D$ disc spacing reaches fully developed turbulence, as assessed by internal intermittency, within the measurement domain.

6. Mapping porous disc wake merging

An interesting finding is that the internal intermittency results for when the turbulence reaches its fully developed state occur farther downstream than the corresponding turbulent spectrum indicator. In the M3.0 and N3.0 cases, the internal intermittency does not decrease back to approximately zero within the measurement domain for scales $\rho = D$.

By comparing the $u'/U(x)$ plots in figure 7 for the centreline measurements with the two differing wake merging results, the streamwise $u'/U(x)$ profiles coincide with the internal intermittency prediction of the wake merging. For both disc designs, the $1.5D$ and $2D$ disc spacing cases reach a $u'/U(x)$-peak and then slowly decay downstream. However, for the N3.0 case, the centreline $u'/U(x)$ plot in figure 7(*a*) reveals that there is no real peak, but rather a plateau that is reached within the measurement domain. For the M3.0 case figure 7(*b*) shows that $u'/U(x)$ barely increases at all within the $40D$ downstream that were measured, and it seems it does not reach a peak within our measurement domain. This corresponds well with the mean streamwise velocity profile in figure 5(*b*) for the M3.0 case, where the mean velocity does not experience a significant deficit. This further indicates that although the wakes might be interacting, they have yet to merge, at least as defined based on the intermittency criterion described herein.

These results illustrate that, while the spectra reach a slope of approximately $-5/3$ in the inertial range, there are still turbulence mechanisms at play which affect the flow. Schwarz *et al.* (2018) showed that, for flows with identical spectra where one has intermittency present and one does not, the intermittent flow causes higher fatigue loading on wind turbines than the non-intermittent flow. Internal intermittency is thus important for understanding wake merging in general, but also specifically when discussing it in relation to wind turbines. As we have shown, internal intermittency is present for a greater downstream distance when compared with most other wake merging criteria.

Table 1 highlights that, although the downstream positions themselves may differ between the disc designs and spacings, the order of turbulence evolution events does not change. A wake map can be found in figure 15, showing the order of events within the flow. The intermittency ring of each wake lies outside the momentum-defined wake, and appears not far downstream from the discs. As Vinnes *et al.* (2023) noted, the occurrence of the intermittency ring is not immediately downstream of the discs. Once the individual intermittency rings meet, the Castaing parameter along the centreline between the two discs at this downstream position increases, indicating wake interaction. This is marked with 'I' in the wake map, and corresponds to our criterion $\lambda^2(\rho = D) > 0.2$. The shear

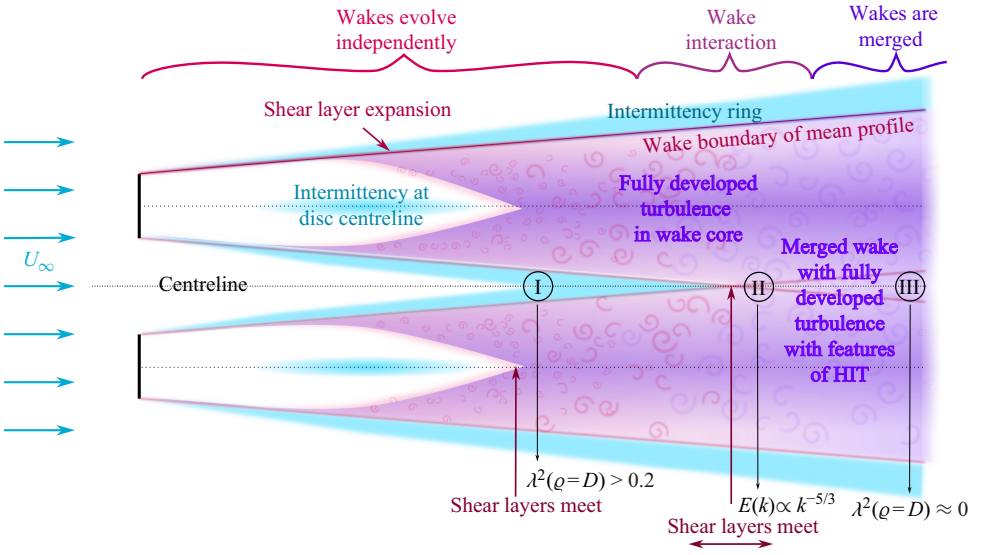

Figure 15. Conceptual wake map. The order of turbulence evolution events is independent of disc design. The three characteristics defined in the work herein are marked with 'I', 'II' and 'III'. The map is not to scale and depends on the disc spacing, and is meant to give the reader a conceptual understanding of what happens in the flow.

layers of the PDs widen (Lignarolo *et al.* 2016), and once they meet, they start interacting. This causes a build-up of the turbulence intensity which eventually reaches a peak. This is similar to the evolution of turbulence in the centre of a single wake (Neunaber 2020). Before this peak, the turbulence has both built up and developed sufficiently for the near –5/3 slope in the turbulence spectrum's inertial range to occur. This is marked with 'II' in the wake map. After $u'/U(x)$ peaks, the turbulence decays downstream until it sufficiently resembles homogeneous isotropic turbulence for the Castaing parameter to have decreased back to approximately zero. This is marked with 'III' in the wake map, and corresponds to the criterion $\lambda^2(\rho = D) \approx 0$. The $u'/U(x)$ decay combined with both spectra that have a near $-5/3$ slope in the inertial range and intermittency only at small spatial scales indicates fully developed turbulence with features of homogeneous isotropic turbulence at this downstream position. Internal intermittency is also found at small spatial scales in the individual wake cores, and the absence of intermittency at the large scales indicates that the flow in these regions is fully developed with features of homogeneous isotropic turbulence. This has been shown for a single wind turbine by Neunaber *et al.* (2020) and a single PD by Neunaber *et al.* (2021). In the $1.5D$ cases, i.e. N1.5 and M1.5, the Castaing parameter exceeds 0.2 at approximately the same downstream position as the wavenumber spectra reach the near $-5/3$ slope.

The present investigation does not explicitly include the addition of background turbulence as it was a study objective to determine how the flow transitions to turbulence and evolves between the two wake-generating objects. Nonetheless, in many flows of practical interest, background turbulence may exist. Studies of the evolution of individual wakes of these PDs in turbulent flows, e.g. Vinnes *et al.* (2023), suggest that the developed conceptual map of wake merging regions is also valid for low and moderate turbulent inflows. In such cases, the expectation is that the wakes will develop more rapidly downstream and merging will occur earlier, but the sequence of events is not

fundamentally different. A difficulty might arise from the identification of the inertial range in the spectra, as the turbulent inflow would already have an inertial range. For very high background turbulence intensities, entrainment may reverse Kankanwadi & Buxton (2020) and the reported map may not hold. At present, we have not explicitly quantified the location of the events as these are dependent on the geometry of the wake-generating object, the spacing and perhaps the inflow conditions.

To summarise, by means of cascading turbulence events at the centreline between two discs, we identify three key indicators of the interaction and merging of two wakes, namely the build-up of intermittency, marked by $\lambda^2(\rho = D) > 0.2$, the convergence of the inertial range of velocity spectra to follow a $-5/3$ decay and the transition to fully developed turbulence with features of homogeneous, isotropic turbulence, marked by $\lambda^2(\rho = D) \approx 0$.

7. Conclusions

The wake merging of and transition to turbulence between side-by-side PDs have been investigated based on three research questions and a repeatable sequence of turbulence events has been identified for different PDs and spacings. Two disc designs were used, namely a non-uniform N-type disc and a mesh disc with uniform blockage, referred to as M-type disc, and three disc spacings were investigated. By defining a series of wake merging criteria, the evolution of wake interaction has been investigated, and a wake map indicating which mechanisms in the flow come into play where has been created. The mean streamwise velocity and u'/U profiles were presented at $8D$ and $30D$ downstream, as well as centreline profiles of the same turbulence characteristics. The centreline measurements were used for identifying when the flow's wavenumber spectrum reached a slope approximately equal to $-5/3$ in the inertial range, and for the evolution of the internal intermittency. It was shown that the turbulence spectra for the N configurations reached this slope farther upstream than the M configurations, and the M configurations were more sensitive to the disc spacing. The Castaing parameter was used to look further into the intermittent events in the flow and wake merging. In the spanwise profiles of the internal intermittency for the dual-disc cases, rings of intermittency could be seen, as previously found by Vinnes *et al.* (2023) for single discs. The centreline measurements were used to determine the start of wake interaction and when the flow became fully developed. The downstream position where the individual rings of intermittency met was defined as the wake-interaction point. Farther downstream the turbulence spectrum reached a near $-5/3$ slope in its inertial region, which was defined as the first indication of developed turbulence. At the end, once the internal intermittency at spatial scale $\rho \approx D$ had decreased back to approximately zero, the flow reached its fully developed far-field state. It is also noted that the internal intermittency of neither $\Delta = 3D$ disc spacing case decreased sufficiently within the measurement domain ($40D$ or 13.3Δ), and therefore, these cases do not exhibit fully developed turbulence within the measurement domain. By looking at the order of events within the flow, a wake map was created. Although the specific events of wake merging occur at different downstream positions for the two discs, the same wake interaction and merging events do occur and they occur in the same order, indicating these phenomena are independent of disc design and suggesting some degree of universality to the process.

Declaration of interests. The authors report no conflict of interest.

Author contributions. F.O.J.B.: Formal analysis; Writing: original draft, Visualisation. R.J.H.: Conceptualisation, Writing: review & editing, Supervision, Funding acquisition. I.N.: Conceptualisation, Methodology, Formal analysis, Investigation, Writing: review & editing, Visualisation, Supervision.

Data availability statement. The CAD drawing of the N disc was made available at DataverseNO, Vinnes *et al.* (2022*a*, *b*), at https://doi.org/10.18710/FFELKX. The data required to reproduce the plots of the present study are available at DataverseNO at: https://doi.org/10.18710/XAEWC5.

Appendix A. Wake superposition

The most basic model for wake merging is superposition of two wakes. While the above results demonstrate that wake merging is a complicated process with a cascading series of events, simple summation of two wake profiles can in some cases capture some of the physics. Contrarily, deviation of the measured results from a basic superposition also identifies where more complex interactions take place. For reference, spanwise profiles of the mean streamwise velocity and turbulence intensity are plotted for all cases herein. Figures 16 and 17 show the profiles at $8D$ for the N and M discs, respectively, and figures 18 and 19 show the profiles for the same discs at $30D$.

At a downstream position of $8D$ and with a spacing of $\Delta = 3D$ the measurements for both N and M discs agree well with basic superposition for both the mean velocity and the turbulence intensity. This is largely because the wakes have not yet met and the two wakes are genuinely developing separately. As the spacing decreases below $\Delta \leqslant 2D$ for the N disc, the measurement deviates from the superposition, indicating that this perspective is insufficient to forecast the side-by-side wake. For the M disc, the superposition still approximately holds – this is because the single wake of the M disc is narrower (figure 4), and hence the wakes have not yet strongly interacted at this measurement position.

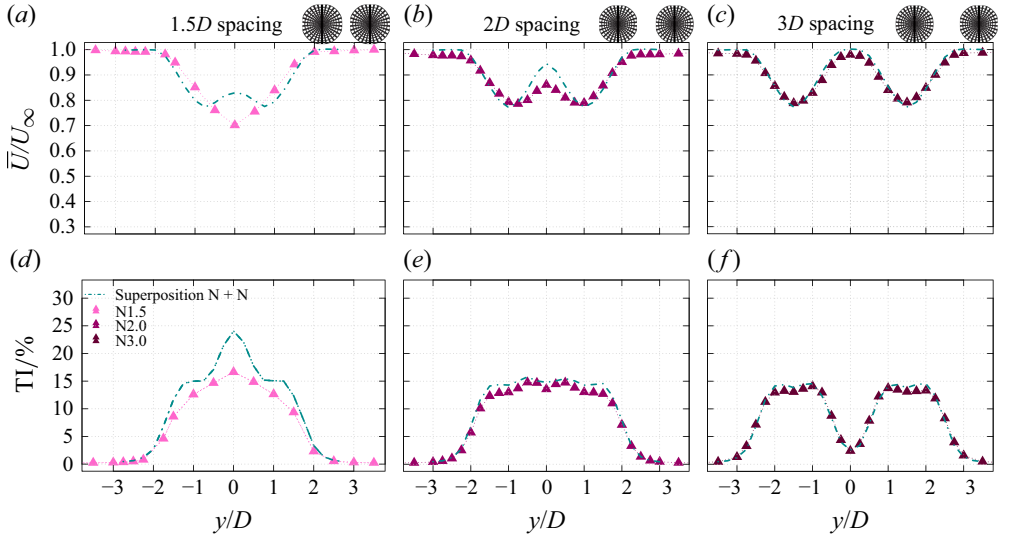

Figure 16. Comparison of the measured wakes downstream of the N type discs at $8D$ with a superposition of the single wakes. Panels (*a*), (*b*) and (*c*) show the normalised mean velocity deficit for cases N1.5, N2.0 and N3.0, respectively, and (*d*), (*e*) and (*f*) show the turbulence intensity for cases N1.5, N2.0 and N3.0.

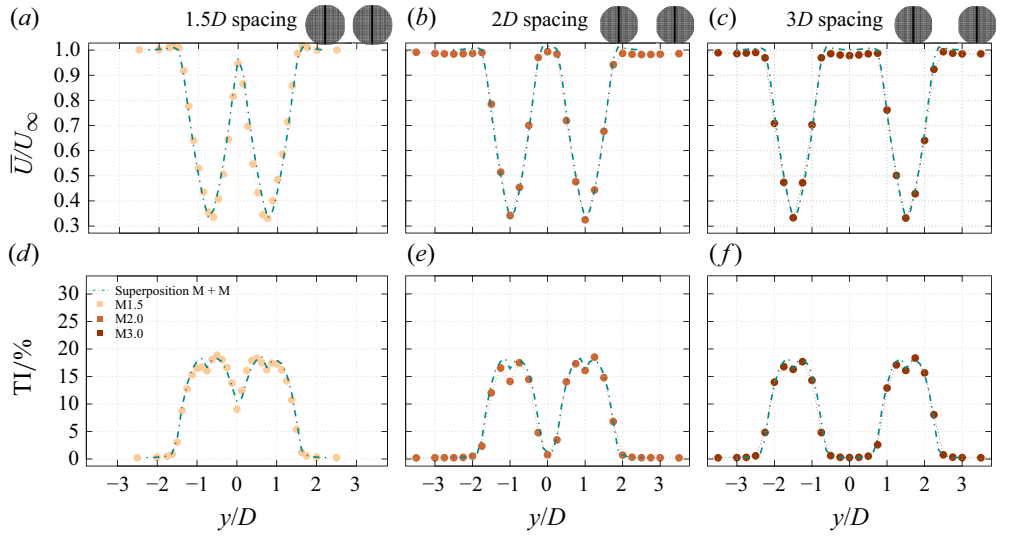

Figure 17. Comparison of the measured wakes downstream of the M type discs at $8D$ with a superposition of the single wakes. Panels (*a*), (*b*) and (*c*) show the normalised mean velocity deficit for cases M1.5, M2.0 and M3.0, respectively, and (*d*), (*e*) and (*f*) show the turbulence intensity for cases M1.5, M2.0 and M3.0.

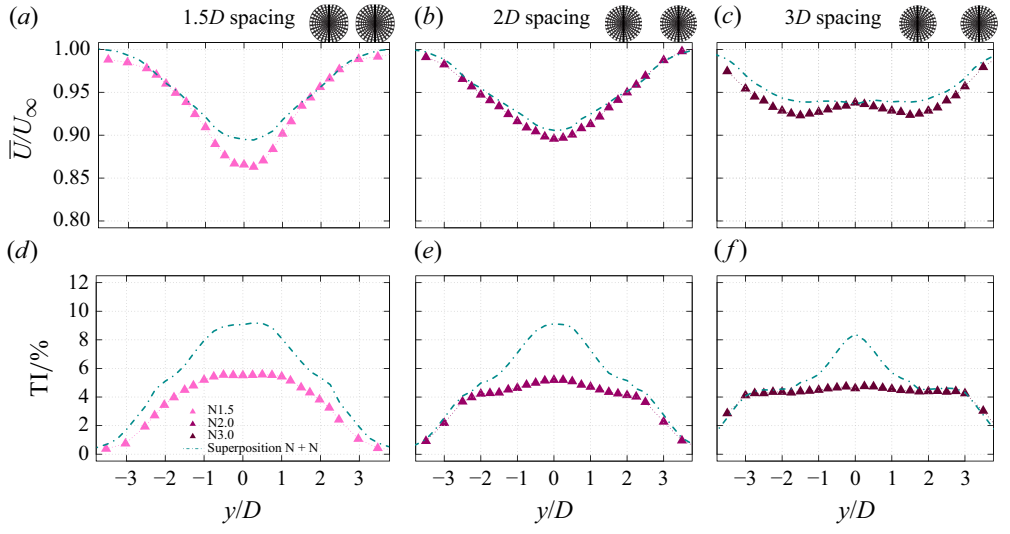

Figure 18. Comparison of the measured wakes downstream of the N type discs at $30D$ with a superposition of the single wakes. Panels (*a*), (*b*) and (*c*) show the normalised mean velocity deficit for cases N1.5, N2.0 and N3.0, respectively, and (*d*), (*e*) and (*f*) show the turbulence intensity for cases N1.5, N2.0 and N3.0.

At 30 downstream, the failure of the superposition is more apparent. While some degree of agreement between superposition and the measurements exists for the M disc wake with $\Delta = 2D$ and $3D$, the turbulence intensity profiles for both discs and all spacings, Δ, demonstrate that superposition overestimates the level of the turbulence fluctuations, particularly at the centreline between the discs.

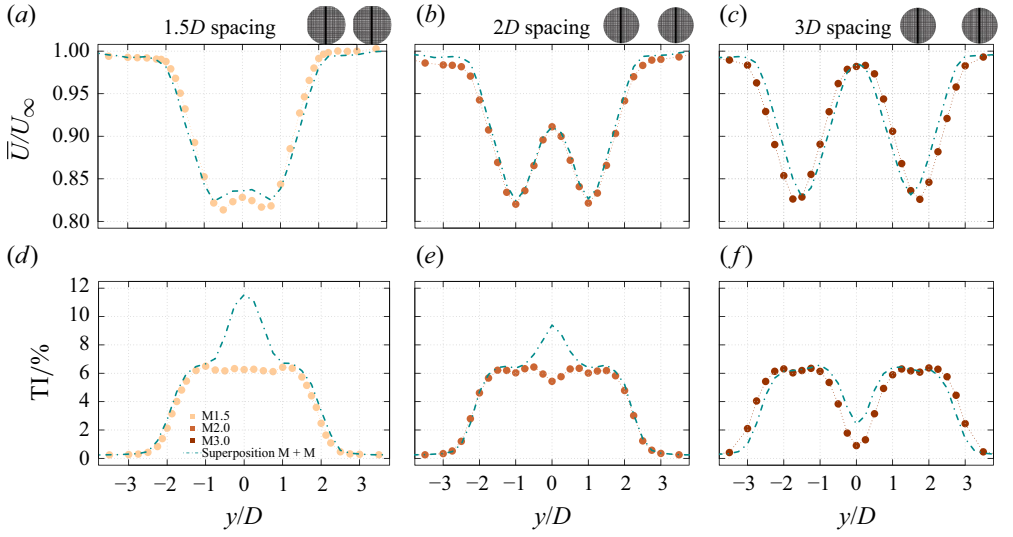

Figure 19. Comparison of the measured wakes downstream of the M type discs at $30D$ with a superposition of the single wakes. Panels (*a*), (*b*) and (*c*) show the normalised mean velocity deficit for cases M1.5, M2.0 and M3.0, respectively, and (*d*), (*e*) and (*f*) show the turbulence intensity for cases M1.5, M2.0 and M3.0.

References

Aubrun, S., Loyer, S., Hancock, P.E. & Hayden, P. 2013 Wind turbine wake properties: comparison between a non-rotating simplified wind turbine model and a rotating model. *J. Wind Engng Ind. Aerodyn.* **120**, 1–8.

Barthelmie, R.J. & Jensen, L.E. 2010 Evaluation of wind farm efficiency and wind turbine wakes at the Nysted offshore wind farm. *Wind Energy* **13** (6), 573–586.

Bastankhah, M. & Abkar, M. 2019 Multirotor wind turbine wakes. *Phys. Fluids* **31** (8), 085106.

Bastankhah, M., Welch, B.L., Martínez-Tossas, L.A., King, J. & Fleming, P. 2021 Analytical solution for the cumulative wake of wind turbines in wind farms. *J. Fluid Mech.* **911**, A53.

Benedict, L. & Gould, R. 1996 Towards better uncertainty estimates for turbulence statistics. *Exp. Fluids* **22** (2), 129–136.

Biswas, N. & Buxton, O.R.H. 2024 Effect of tip speed ratio on coherent dynamics in the near wake of a model wind turbine. *J. Fluid Mech.* **979**, A34.

Bossuyt, J., Meneveau, C. & Meyers, J. 2018 Effect of layout on asymptotic boundary layer regime in deep wind farms. *Phys. Revi. Fluids* **3** (12), 124603.

Bourhis, M. & Buxton, O.R.H. 2024 Influence of freestream turbulence and porosity on porous disk-generated wakes. *Phys. Rev. Fluids* **9** (12), 124501.

Brown, G.L. & Roshko, A. 2012 Turbulent shear layers and wakes. *J. Turbul.* **13**, N51.

Camp, E.H. & Cal, R.B. 2016 Mean kinetic energy transport and event classification in a model wind turbine array versus an array of porous disks: energy budget and octant analysis. *Phys. Rev. Fluids* **1** (4), 044404.

Castaing, B., Gagne, Y. & Hopfinger, E.J. 1990 Velocity probability density functions of high Reynolds number turbulence. *Physica D: Nonlinear Phenom.* **46** (2), 177–200.

Castro, I.P. 1971 Wake characteristics of two-dimensional perforated plates normal to an air-stream. *J. Fluid Mech.* **46** (3), 599–609.

Chilla, F., Peinke, J. & Castaing, B. 1996 Multiplicative process in turbulent velocity statistics: a simplified analysis. *J. Phys. II* **6** (4), 455–460.

Cicolin, M.M., Buxton, O.R.H., Assi, G.R.S. & Bearman, P.W. 2021 The role of separation on the forces acting on a circular cylinder with a control rod. *J. Fluid Mech.* **915**, A33.

Cicolin, M.M., Chellini, S., Usherwood, B., Ganapathisubramani, B. & Castro, I.P. 2024 Vortex shedding behind porous flat plates normal to the flow. *J. Fluid Mech.* **985**, A40.

Dadmarzi, F.H., Narasimhamurthy, V.D., Andersson, H.I. & Pettersen, B. 2018 Turbulent wake behind side-by-side flat plates: computational study of interference effects. *J. Fluid Mech.* **855**, 1040–1073.

España, G., Aubrun, S., Loyer, S. & Devinant, P. 2011 Spatial study of the wake meandering using modelled wind turbines in a wind tunnel. *Wind Energy* **14** (7), 923–937.

ESPAÑA, G., AUBRUN, S., LOYER, S. & DEVINANT, P. 2012 Wind tunnel study of the wake meandering downstream of a modelled wind turbine as an effect of large scale turbulent eddies. *J. Wind Eng. Ind. Aerodyn.* **101**, 24–33.

FRISCH, U. 1995 *Turbulence: The Legacy of AN Kolmogorov*. Cambridge University Press.

FUCHS, A., KHARCHE, S., PATIL, A., FRIEDRICH, J., WÄCHTER, M. & PEINKE, J. 2022 An open source package to perform basic and advanced statistical analysis of turbulence data and other complex systems. *Phys. Fluids* **34** (10), 101801.

GAMBUZZA, S. & GANAPATHISUBRAMANI, B. 2023 The influence of free stream turbulence on the development of a wind turbine wake. *J. Fluid Mech.* **963**, A19.

GARCIA, E.T., AUBRUN, S., COUPIAC, O., GIRARD, N. & BOQUET, M. 2019 Statistical characteristics of interacting wind turbine wakes from a 7-month LiDAR measurement campaign. *Renew. Energy* **130**, 1–11.

HEARST, R.J., BUXTON, O.R.H., GANAPATHISUBRAMANI, B. & LAVOIE, P. 2012 Experimental estimation of fluctuating velocity and scalar gradients in turbulence. *Exp. Fluids* **53** (4), 925–942.

HELVIG, S., VINNES, M.K., SEGALINI, A., WORTH, N.A. & HEARST, R.J. 2021 A comparison of lab-scale free rotating wind turbines and actuator disks. *J. Wind Engng Ind. Aerodyn.* **209**, 104485.

HULTMARK, M. & SMITS, A.J. 2010 Temperature corrections for constant temperature and constant current hot-wire anemometers. *Meas. Sci. Technol.* **21** (10), 105404.

JACKSON, R.S. & AMANO, R. 2017 Experimental study and simulation of a small-scale horizontal-axis wind turbine. *J. Energy Res. Technol.* **139** (5), 051207.

KANKANWADI, K.S. & BUXTON, O.R.H. 2020 Turbulent entrainment into a cylinder wake from a turbulent background. *J. Fluid Mech.* **905**, A35.

KATIC, I., HØJSTRUP, J. & JENSEN, N.O. 1987 A simple model for cluster efficiency. In *European Wind Energy Association Conference and Exhibition*, pp. 407–410. A. Raguzzi.

KURELEK, J.W., PIQUÉ, A. & HULTMARK, M. 2023 Performance of the porous disk wind turbine model at a high Reynolds number: Solidity distribution and length scales effects. *J. Wind Engng Ind. Aerodyn.* **237**, 105377.

LI, L., HEARST, R.J., FERREIRA, M.A. & GANAPATHISUBRAMANI, B. 2020 The near-field of a lab-scale wind turbine in tailored turbulent shear flows. *Renew. Energy* **149**, 735–748.

LIGNAROLO, L.E.M., RAGNI, D., FERREIRA, C.J. & VAN BUSSEL, G.J.W. 2016 Experimental comparison of a wind-turbine and of an actuator-disc near wake. *J. Renew. Sustain. Ener.* **8** (2), 023301.

LISSAMAN, P.B.S. 1979 Energy effectiveness of arbitrary arrays of wind turbines. *J. Energy* **3** (6), 323–328.

MAUS, J., PEINKE, J. & HÖLLING, M. 2022 Experimental investigation on the effect of lateral turbine spacing on interactions of wakes. *J. Phys. Conf. Ser.* **2265**, 042064.

MESSMER, T., HÖLLING, M. & PEINKE, J. 2024 Enhanced recovery caused by nonlinear dynamics in the wake of a floating offshore wind turbine. *J. Fluid Mech.* **984**, A66.

MI, J., DEO, R.C. & NATHAN, G.J. 2005 Fast-convergent iterative scheme for filtering velocity signals and finding Kolmogorov scales. *Phys. Rev. E* **71** (6), 066304.

MI, J., XU, M. & DU, C. 2011 Digital filter for hot-wire measurements of small-scale turbulence properties. *Meas. Sci. Technol.* **22** (12), 125401.

NAERT, A., PUECH, L., CHABAUD, B., PEINKE, J., CASTAING, B. & HEBRAL, B. 1994 Velocity intermittency in turbulence: how to objectively characterize it? *J. Phys. II* **4** (2), 215–224.

NEUNABER, I. 2019 Stochastic investigation of the evolution of small-scale turbulence in the wake of a wind turbine exposed to different inflow conditions. PhD thesis, Carl von Ossietzky Universität Oldenburg, Germany.

NEUNABER, I. 2020 *Turbulence of Wakes*. Springer International Publishing.

NEUNABER, I., HÖLLING, M., STEVENS, R.J.A.M., SCHEPERS, G. & PEINKE, J. 2020 Distinct turbulent regions in the wake of a wind turbine and their inflow-dependent locations: the creation of a wake map. *Energies* **13** (20), 5392.

NEUNABER, I., HÖLLING, M., WHALE, J. & PEINKE, J. 2021 Comparison of the turbulence in the wakes of an actuator disc and a model wind turbine by higher order statistics: a wind tunnel study. *Renew. Energy* **179**, 1650–1662.

NIAYIFAR, A. & PORTÉ-AGEL, F. 2016 Analytical modeling of wind farms: a new approach for power prediction. *Energies* **9** (9), 741.

OBLIGADO, M., DAIRAY, T. & VASSILICOS, J.C. 2016 Non-equilibrium scaling of turbulent wakes. *Phys. Rev. Fluids* **1** (4), 044409.

OBLIGADO, M., KLEIN, S. & VASSILICOS, J.C. 2022 Interaction of two axisymmetric turbulent wakes. *Phys. Rev. Fluids* **7** (11), 114606.

PEINKE, J., KLEIN, M., KITTEL, A., OKNINSKY, A., PARISI, J. & ROESSLER, O.E. 1993 On chaos, fractals and turbulence. *Phys. Scr.* **1993** (T49B), 672–676.

PIERELLA, F. & SÆTRAN, L. 2017 Wind tunnel investigation on the effect of the turbine tower on wind turbines wake symmetry. *Wind Energy* **20** (10), 1753–1769.
POPE, S.B. 2000 *Turbulent Flows*. Cambridge University Press.
SCHOTTLER, J., BARTL, J., MÜHLE, F., SÆTRAN, L., PEINKE, J. & HÖLLING, M. 2018 Wind tunnel experiments on wind turbine wakes in yaw: redefining the wake width. *Wind Energy Sci.* **3** (1), 257–273.
SCHÜMANN, H., PIERELLA, F. & SÆTRAN, L. 2013 Experimental investigation of wind turbine wakes in the wind tunnel. *Energy Procedia* **35**, 285–296.
SCHWARZ, C.M., EHRICH, S., MARTÍN, R. & PEINKE, J. 2018 Fatigue load estimations of intermittent wind dynamics based on a blade element momentum method, *J. Phys.: Conf. Ser.* **1037**, 072040.
SCOTT, R., VIGGIANO, B., DIB, T., ALI, N., HÖLLING, M., PEINKE, J. & CAL, R.B. 2020 Wind turbine partial wake merging description and quantification. *Wind Energy* **23** (7), 1610–1618.
STEIROS, K., OBLIGADO, M., BRAGANÇA, P., CUVIER, C. & VASSILICOS, J.C. 2025 Turbulent shear flow without vortex shedding, reynolds shear stress and small-scale intermittency. *J. Fluid Mech.* **1002**, A51.
STRYKOWSKI, P.J. & SREENIVASAN, K.R. 1990 On the formation and suppression of vortex 'shedding' at low Reynolds numbers. *J. Fluid Mech.* **218**, 71–107.
SUMNER, D. 2010 Two circular cylinders in cross-flow: a review. *J. Fluids Struct.* **26** (6), 849–899.
TENNEKES, H. & LUMLEY, J.L. 1972 *A First Course in Turbulence*. MIT press.
THEUNISSEN, R., ALLEN, C.B. & HOUSLEY, P. 2015 On the feasibility of using porous discs for wind tunnel simulations of wind farm power variation with turbine layout. In *33rd Wind Energy Symposium*, p. 0222. AIAA.
THOMSEN, K. & SØRENSEN, P. 1999 Fatigue loads for wind turbines operating in wakes. *J. Wind Engng Ind. Aerodyn.* **80** (1–2), 121–136.
TOSCHI, F., AMATI, G., SUCCI, S., BENZI, R. & PIVA, R. 1999 Intermittency and structure functions in channel flow turbulence. *Phys. Rev. Lett.* **82** (25), 5044–5047.
VAD, A., TAMARO, S. & BOTTASSO, C.L. 2023 A non-symmetric Gaussian wake model for lateral wake-to-wake interactions, *J. Phys.: Conf. Ser.* **2505**, 012046.
VINNES, M.K., GAMBUZZA, S., GANAPATHISUBRAMANI, B. & HEARST, R.J. 2022*a* The far wake of porous disks and a model wind turbine: Similarities and differences assessed by hot-wire anemometry. *J. Renew. Sustain. Energy* **14** (2), 023304.
VINNES, M.K., GAMBUZZA, S., GANAPATHISUBRAMANI, B. & HEARST, R.J. 2022*b* 'nd.stp' – replication data for: the far wake of porous disks and a model wind turbine: similarities and differences assessed *b*y hot wire anemometry. *DataverseNO* **V1**, Accessed online: 24th of March 2025.
VINNES, M.K., NEUNABER, I., LYKKE, H.-M.H. & HEARST, R.J. 2023 Characterizing porous disk wakes in different turbulent inflow conditions with higher-order statistics. *Exp. Fluids* **64** (2), 25.
VOUTSINAS, S., RADOS, K. & ZERVOS, A. 1990 On the analysis of wake effects in wind parks. *Wind Engng* 204–219.
WU, Y.-T. & PORTÉ-AGEL, F. 2012 Atmospheric turbulence effects on wind-turbine wakes: an les study. *Energies* **5** (12), 5340–5362.
ZDRAVKOVICH, M.M. 1977 Review of flow interference between two circular cylinders in various arrangements. *J. Fluids Engng* **99** (4), 618–633.
ZHOU, Y., MAHBUB ALAM, M. 2016 Wake of two interacting circular cylinders: a review. *Intl J. Heat Fluid Flow* **62**, 510–537.
ZONG, H. & PORTÉ-AGEL, F. 2020 A momentum-conserving wake superposition method for wind farm power prediction. *J. Fluid Mech.* **889**, A8.